Swarm and Evolutionary Computation 95 (2025) 101953

Contents lists available at ScienceDirect

Swarm and Evolutionary Computation

journal homepage: www.elsevier.com/locate/swevo

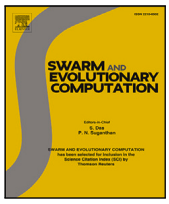

# Methodology for optimizing electrical grounding grids in stratified soils using advanced calculation techniques and evolutionary algorithms

Carlos Leandro Borges da Silva [a,g,*], Thyago Gumeratto Pires [a,g], Antonio Marcelino Silva Filho [a,d,g], Junio Santos Bulhões [a,f,g], Orlando M. Oliveira Belo [c], Clóves Gonçalves Rodrigues [e], Antonio Paulo Coimbra [b], Wesley Pacheco Calixto [a,b,g,**]

[a] Electrical, Mechanical & Computer Engineering School, Federal University of Goias, Goiania, Goias, PC 74.605-220, Brazil
[b] Institute of Systems and Robotics, Coimbra University, Coimbra, PC 3030-290, Portugal
[c] Department of Informatics, School of Engineering, University of Minho, Braga, PC 4710-057, Portugal
[d] Electrical Power Systems Study Group, Federal Institute of Tocantins, Palmas, Tocantins, PC 77.021-090, Brazil
[e] Graduate Program in Production and Systems Engineering, Pontifical Catholic University of Goias, Goiania, Goias, PC 74605-010, Brazil
[f] Federal Institute of Mato Grosso (IFMT), Mato Grosso, Brazil
[g] Technology Research and Development Center, Federal Institute of Goias, Goiania, Goias, PC 74.055-110, Brazil

## ARTICLE INFO

*Keywords:*
Evolutionary algorithms
Optimization of electrical grounding
System modeling
Resilient infrastructure
Industrial automation systems

## ABSTRACT

This paper presents a practical methodology for optimizing the geometry of electrical grounding grids at industrial frequencies of 50 Hz and 60 Hz, integrating advanced calculation techniques and evolutionary algorithms to improve the safety and operational performance of electrical grounding systems. The proposed approach is particularly beneficial for industrial automation and control systems, where effective grounding is necessary to maintain system reliability and prevent downtime. This methodology employs mathematical modeling and computational tools to optimize grid parameters, ensuring compliance with safety standards while reducing operational costs, thus contributing to the overall efficiency of automated systems in industrial environments. The study reports a reduction of up to 66% in the number of vertical rods and 40% in horizontal conductors compared to traditional methods. These results indicate that the proposed methodology can significantly reduce material usage and costs while maintaining electrical safety in accordance with regulatory standards, making it applicable to a wide range of industrial settings, including substations and automated facilities.

## 1. Introduction

The design of grounding grids at industrial frequencies of 50 Hz and 60 Hz must consider both grounding resistance and human safety, which is associated with the distribution of surface potential [1]. Classical methods are widely used for the calculation and design of these grids, however, they have limitations in accurately representing soil heterogeneity and surface potential distribution. Furthermore, they are generally restricted to simple geometries, such as square, rectangular, L-shaped, and T-shaped grids [2], which may be inadequate for complex industrial environments.

Soil heterogeneity introduces uncertainties in the performance of grounding grids, particularly in environments subject to seasonal variations in resistivity [3]. These fluctuations can increase grounding resistance and hinder the dissipation of the fault current, requiring adaptive strategies to ensure compliance with safety regulations [4,5]. Extreme conditions, such as subzero temperatures, intensify these effects, reducing the reliability of the system. Furthermore, non-homogeneous soils require specialized methodologies to ensure proper distribution of surface potential and prevent localized overvoltages [6,7].

Optimization techniques combining computational intelligence and numerical methods improve the adaptability of grounding systems to different soil conditions. Simulated annealing (MSA) and random walk methods adjust grid configurations while minimizing material costs and maintaining compliance with safety standards [6,8]. Although uniform arrangements are suitable for standardized conditions, non-uniform configurations have demonstrated higher efficiency in multilayered soils [9]. Furthermore, in high-resistivity environments with limited

* Corresponding author.
** Corresponding author at: Institute of Systems and Robotics, Coimbra University, Coimbra, PC 3030-290, Portugal.
*E-mail addresses:* carlosleandro82@ufg.br (C.L.B.d. Silva), marcelino.filho@ifto.edu.br (A.M. Silva Filho), wesley.pacheco@ufg.br (W.P. Calixto).

https://doi.org/10.1016/j.swevo.2025.101953
Received 23 October 2024; Received in revised form 2 April 2025; Accepted 14 April 2025
Available online 30 April 2025

space, hybrid approaches, such as chemical electrodes and soil enhancement materials, have yielded promising results [3,10]. These strategies enable more flexible and cost-effective grounding designs compared to conventional methodologies.

Computational models, such as the Boundary Element Method (BEM) and the Finite Element Method (FEM), offer advantages in modeling stratified soils, addressing limitations of traditional analytical techniques [11,12]. Hybrid approaches that integrate FEM and neural networks improve computational efficiency in large-scale grounding simulations [13]. Furthermore, computational simulations are used to assess the influence of soil heterogeneity on grounding resistance [14], while hybrid techniques that incorporate FEM enable more detailed analyzes of non-homogeneous soils [15]. Furthermore, circuit-based models highlight the limitations of classical equipotentiality assumptions [16].

Advancements in computational modeling have led to refined optimization techniques to improve grounding grid performance. Habjanic & Trlep [17] applied finite element methods to optimize horizontal electrode spacing, minimizing touch and step voltages without altering conductor length, demonstrating improved efficiency in heterogeneous soils [18]. Uma et al. [19] used finite element models to refine grid geometries, focusing on cost reduction while ensuring compliance with safety limits. Sherif & Ibrahim [20] proposed an evolutionary algorithm to optimize the spacing between horizontal conductors and the total grid size, leading to notable reductions in both costs and step and touch voltages. Gouda et al. [21] furthered this approach by integrating the optimal compression ratio with particle swarm optimization (PSO), achieving up to a 20% reduction in total conductor length.

The development of optimization techniques has led to a growing emphasis on evolutionary and heuristic methods to improve grounding grid design, ensuring regulatory compliance while reducing installation costs. These approaches provide cost savings exceeding 29% compared to conventional methods [22]. Evolutionary algorithms, such as genetic algorithms (GA), particle swarm optimization (PSO), and gravitational search algorithm (GSA), refine the placement and spacing of conductors to improve efficiency [22,23]. In addition, some studies incorporate soil-specific models and parameters – including conductor dimensions and installation depth – to further optimize performance under varying geological conditions [8,24,25]. Using heuristic techniques, these methods adapt to complex terrain geometries, offering solutions more efficient than traditional design methodologies.

Artificial intelligence has been increasingly applied in grounding grid optimization, enabling configurations that minimize step and touch voltages while reducing material consumption [23,26]. These approaches improve adaptability by accounting for variations in soil heterogeneity and resistivity [23,26]. Genetic algorithms and evolutionary strategies refine the placement of the conductors, ensuring a more uniform potential distribution [23,26]. Furthermore, simulated annealing has improved grounding configurations by reducing dependence on extensive horizontal conductors and vertical electrodes while ensuring regulatory compliance [24,27]. The integration of artificial intelligence enables automated adjustments based on soil conditions, enhancing efficiency without the need for manual recalibration [28,29].

These strategies have been applied to optimize grid dimensions, considering step and touch voltages in homogeneous and two-layer soils [20,30]. The MSA has been used to improve grounding configurations in various soil conditions, reducing the need for conductors and vertical electrodes while maintaining compliance with regulatory standards [24,27]. Furthermore, the integration of GA has allowed a more precise determination of the grid geometry and parameters for different soil types [28,29].

Several mathematical methodologies have been explored to optimize grounding grids, ensuring both efficiency and regulatory compliance [8,31,32]. Techniques such as mixed-integer linear programming, gradient descent, and random walk algorithms have been applied to improve the cost-benefit ratio of grid design [22,33]. Recent studies integrate computational simulations with field measurements to validate the actual performance of optimized grounding systems [34,35]. These approaches have been particularly valuable in urban environments, where space constraints and soil characteristics impose additional design challenges. The ability to combine heuristic and mathematical methods allows for more adaptive and site-specific grid configurations, improving reliability in varying conditions.

While modern optimization techniques offer significant advancements, traditional methods remain valuable for grounding grid analysis. Dwight [36] introduced the average potential method, originally developed by Howe [37], to calculate the contribution of electrode-induced potentials and their reflections on the soil surface. Sverak [38] demonstrated that the IEEE Guide for Safety in AC Substation Grounding (GSSG-IEEE) [2] has limitations in evaluating potential profiles, particularly at the edges of the grid. However, his refinements improve the accuracy for varying the conductor spacing. Heppe [39] proposed the complex image method, which accommodates electrodes with different orientations, but its application remains restricted to square grids with uniformly spaced conductors. In contrast, Kouteynikoff's approach [40] enhances the representation of horizontal conductors in the analysis of the grounding grid, improving the evaluation of potential distribution under fault conditions. These classical methods, despite their limitations, provide foundational insights that support modern computational advancements.

Heppe [39] proposes the conventional image method, which allows the calculation of surface potentials for electrodes with any angular orientation. Although this method offers advantages, such as accommodating electrodes in different soil layers, it is limited to square grids with equally spaced parallel and perpendicular electrodes. In contrast, Kouteynikoff's methodology [40] enables a more accurate representation of horizontal cables in grounding grid analysis, optimizing step and touch voltages during ground faults. Garrett & Pruitt [41] developed a sensitivity analysis to identify issues with the average potential method, showing that significant errors can occur when assuming a uniform surface potential in the grounding grid. Takahashi & Kawase [42] develop a theoretical approach to calculate the resistance to grounding of vertical rods that penetrate heterogeneous soils, allowing designers to determine the appropriate rod length to achieve the desired resistance in the grid.

Dawalibi & Barbeito [43] compare computational methods with practical measurements with grounding grids in heterogeneous soils. Their results show that when considering stratified soil layers, computational methods provide more accurate results compared to homogeneous soils. Chow & Salama [44] propose a mathematical expression based on dividing the area of the grid into sub-grids, which produces better results compared to other methods, such as those of Dawalibi & Barbeito. Elsherbiny et al. [45] focus on grids composed solely of vertical rods in two-layer soils, simplifying resistance calculations by dividing the grid into two segments. Pires et al. [46], using complex image methods and average potential, extend these concepts to more complex geometries but limit their results to horizontal grids.

Expanding the application of these mathematical and computational models, recent research advances the optimization of grounding grids, particularly in industrial environments where electrical safety and cost reduction are priorities. In facilities such as automated factories and petrochemical plants, which have a high density of electronic equipment, inadequate grounding can cause electromagnetic interference, sensor failures, and disruption of control systems [23]. To address these challenges, advanced optimization methods have been applied to ensure efficient dissipation of fault currents while maintaining compliance with industrial safety regulations [47].

Beyond industrial facilities, the rapid digital transformation and integration of smart grids further reinforce the need for grounding optimization, as electrical failures can disrupt automated processes and cause significant financial losses. In the telecommunications sector,

semiconductor manufacturing and high-precision industries, grounding grid optimization is applied to minimize interference and ensure the stability of sensitive equipment [31,35]. The resistance of the grounding grid is strongly influenced by soil heterogeneity and seasonal variations [4,5]. To mitigate these effects, research indicates that the use of low-resistivity materials and chemical electrodes enhances grounding performance, reduces energy dissipation, and ensures greater electrical stability under varying environmental conditions [3,48].

In addition to material-based solutions, modifying the geometric configuration of the grounding grid can also mitigate the adverse effects of soil heterogeneity and environmental fluctuations. Recent studies indicate that adapting the grid geometry to the shape of the installation area [49], along with the use of non-uniformly spaced electrodes [50], contributes to a more uniform distribution of surface potential, reducing voltage gradients that can compromise safety. To achieve this, it is essential to consider variables such as soil resistivity, layer thickness, and possible irregularities in grid configuration [26,51]. The use of response surfaces combined with optimization methods has allowed the reduction of the number of conductors without compromising the required safety levels [52]. Evolutionary strategies are applied to optimize grid dimensions, allowing material cost reduction while ensuring efficient dissipation of fault currents into the soil [20,27,30].

Although advanced optimization techniques have been extensively investigated, gaps remain in the literature on adaptation of the geometries of the grounding grid to different soil configurations and variations in conductor angulation. This study aims to develop computational methods that improve these adaptations, ensuring greater efficiency and reducing operational costs. The justification for this work lies in the need to design grounding systems that minimize costs while improving safety and optimizing the grid for various installation geometries. The central hypothesis is that by optimizing the geometry of the grounding grid—considering horizontal conductors with varied angles and unequal spacings, along with vertical rods positioned at any point within the structure, it is possible to determine the optimal parameters for the design. This will lead to a more efficient, safer and cost-effective system, even in heterogeneous and stratified soils.

The proposed methodology integrates advanced mathematical computational modeling with evolutionary optimization techniques to improve the design of the ground grid. In addition to minimizing electrical interference and reducing costs, this approach is essential for the electrical sector, which requires resilient and adaptable solutions to varying soil conditions. Therefore, this study presents a solution that combines precision, efficiency, and practical feasibility for industrial applications and electrical infrastructure.

The originality of this work lies in the development of a methodology that optimizes grounding grids for any terrain geometry, taking into account horizontal conductors with varied angles and vertical rods in different positions, an aspect not widely addressed in the existing literature. The innovation of the study is highlighted by the application of optimization techniques to unconventional grounding grid geometries, a topic not explored in previous studies. The relevance of this work to academia, among others, is in providing a computational tool that improves safety and reduces costs in grounding system design, applicable in both industrial settings and substations.

In terms of feasibility, the proposed method offers advantages by reducing the construction costs of grounding grids and reducing the time required for implementation, making it financially accessible. Finally, the applicability of this work is broad, as it can be used in grounding projects for electrical installations, substations, industries, and any other situations where ensuring electrical safety through efficient and cost-effective grounding grids is necessary. This study is organized as follows: Section 2 presents the theoretical foundation, covering necessary concepts such as soil stratification, the effect of asymmetric fault currents, the current applied to the grounding grid, and the increase in the potential of the grid, all of which are important for understanding the methodology and analyzing the results. Section 3 details the proposed methodology, from model construction to result acquisition. Section 4 is dedicated to the discussion of the results, and Section 5 presents the conclusions of the study.

## 2. Theoretical background

This section presents the concepts of stratification of the soil into horizontal layers, fault current, and the effect of asymmetric fault currents. The parameters and potentials of the grounding grids in homogeneous and stratified soils are discussed, along with resistances and potentials in segments of stratified and homogeneous soil.

### 2.1. Soil stratification and optimization in grounding grid design

Soil stratification is a fundamental factor in the design of grounding grids, particularly in heterogeneous soils, which exhibit significant variations in electrical resistivity both seasonally and with depth [3]. However, key soil characteristics, such as the presence of overlapping layers, are often overlooked in the design of the grounding system. Simplified representations that model the soil as a single layer may lead to grids that do not meet safety requirements because they disregard critical variations in electrical resistivity with depth. These variations directly influence current dissipation and surface potential distribution, which could result in step and touch voltages exceeding acceptable limits [53]. Thus, equivalent models that account for mathematical complexity, measurement accuracy, and computational objectives become necessary [25,54]. For soils with up to two layers, graphical methods, simplified approaches, and optimization techniques are commonly employed. In cases where soils contain more than two layers, techniques such as Pirson's method, Yokogawa's diagram, and three-dimensional stratification are recommended [29].

In the two-layer stratification model described by Calixto et al. [29], the upper layer has a resistivity of $\rho_1$ and a thickness of $h_1$, while the lower layer has a resistivity of $\rho_2$ and an infinite depth. The apparent resistivity of the stratified soil is calculated as the sum of the contributions of each layer, considering the reflection coefficient $K$, which depends on the difference in resistivities between layers [55]. This model allows for the determination of parameters such as $K$ and $h_1$, which are necessary for the accurate analysis and design of the grounding grid, ensuring that resistivity values are appropriate for the safety and efficiency of the system.

Furthermore, the concept of optimization is applied to adjust the apparent resistivity curves obtained experimentally and theoretically. This process aims to minimize the evaluation function, providing the optimal values for $\rho_1$, $K$, and $h_1$, ensuring that the soil stratification model accurately reflects the actual ground conditions [55]. This method is particularly useful when greater accuracy is required in soils with complex characteristics [29].

### 2.2. Fault current analysis and its impact on grounding grids

A fault current occurs when there is contact or an arc between parts of the electrical system at different potentials or with the ground, resulting in current flow from one conductor to another or to the ground. These faults typically arise from short circuits that can be symmetrical or asymmetrical. In a symmetrical short circuit, the resultant currents cancel out, whereas in an asymmetrical short circuit, particularly in single-phase and double-phase faults with ground contact, the *zero*-sequence current $I_0$ becomes significant, directly affecting the current applied to the grounding grid [54,56–58].

The *zero* sequence current is an important factor in fault current analysis and is calculated based on the type of short circuit. For double phase short circuits with ground contact, the expression for determining $I_0$ depends on parameters such as the resistances and reactances of the positive, negative and *zero*-sequences. In the case of single-phase short

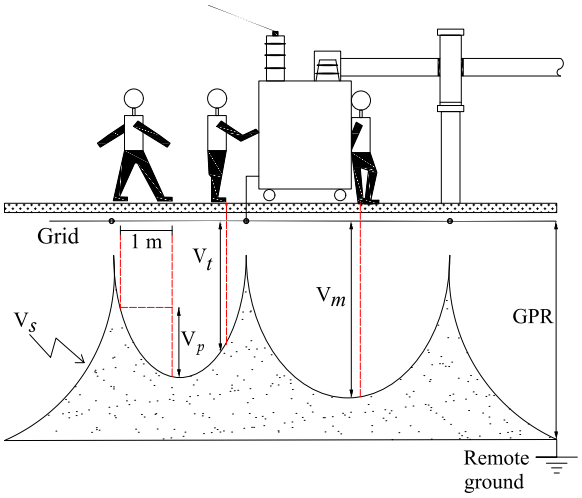


**Fig. 1.** Representation of touch voltage, step voltage and GPR.

circuits, the *zero*-sequence current is calculated considering the estimated fault resistance and the system reactances [2]. These expressions can be simplified in certain situations, such as disregarding the system's equivalent resistance, without a significant loss of accuracy.

The effect of asymmetric current must be considered, as it includes subtransient, transient, and steady-state components, in addition to the DC component. The effective current, which accounts for the decay factor $D_f$, is calculated to determine the total current applied to the grounding grid. This current value, which can range from 10% to 64% of the short-circuit current, is necessary for the proper size of the grid, ensuring that the touch and step potentials remain within safe limits [2,56,57].

### 2.3. Grounding grid parameters and potential calculations

Grounding grid parameters are necessary to define its functionality and safety, especially during ground faults. Ground Potential Rise (GPR) occurs when a fault current is carried through the grid, increasing the electrical potential relative to the remote ground. This increase is directly proportional to the injected current and ground resistance [56,57]. The touch and step voltages are important measurements: the touch voltage represents the potential difference between the ground and a grounded metallic structure within reach of the arm, while the step voltage is the potential difference on the ground surface between a person's feet, separated one meter apart [2]. Both voltages must be kept within safe limits to prevent electric shock hazards, as defined by current standards. Fig. 1, adapted from Asser [59], illustrates key parameters during ground faults, where $V_s$ is the surface potential in the person's location, $V_p$ is the step voltage, $V_t$ is the touch voltage, $V_m$ is the maximum touch voltage within the grid, and GPR is the increase in ground potential.

The resistance of the electrical grounding grid is another important parameter, consisting of the electrode resistances, the soil interface, and the surrounding soil [60,61]. In power systems operating at low frequencies, resistance dominates the total impedance of the grid because of the soil's electrical resistivity. The resistance of the grid is calculated by dividing the GPR by the total current injected into the grid and is influenced by the resistivity of the soil and the length of the electrode.

The electrical potential on the surface of homogeneous soil is calculated considering a point or linear current source. In homogeneous media, the potential is influenced by the resistivity of the soil and the distance from the current source [62]. The expression that describes the resulting potential at a point on the soil surface accounts for the dispersion of current and the distribution of waves emitted and reflected by the source [63]. Analyzing these potentials allows for evaluating the efficiency of the grounding grid in homogeneous soils.

Fig. 2 illustrates a point current source $F$ placed in Medium 1 and a point $P$ at a distance from the source, where $F'$ is the image of the current source, $\rho_1$ is the apparent electrical resistivity of the first soil layer, $\rho_2$ is the apparent electrical resistivity of the second soil layer, $E_e$ and $J_e$ are the magnitudes of the waves emitted by the source that directly hit the plane or point in the same layer as the source, $E_r$ and $J_r$ are the magnitudes of the waves reflected on plane $Q$, $E_f$ and $J_f$ are the magnitudes of the waves refracted into Medium 2, $r'_0$ is the distance between the symmetrical image of the point source and point $P$ on the soil, and $r_0$ is the distance between the point current source and point $P$ on the soil.

The maximum potential generated by the grounding system during a fault should not result in a shock current exceeding the limit established by Dalziel [64]. At the substation, the grounding grid is covered with a layer of gravel to increase resistance to contact between the ground and the feet. The gravel acts as an additional resistive layer on the soil surface. Therefore, it is necessary to adjust the parameter $\rho_s$ to account for the presence of the gravel layer when calculating the maximum touch voltage in (1) and the maximum step voltage in (2), where $\rho_s$ is the resistivity of the surface material, $t$ is the duration of the fault, $h_s$ is the thickness of the gravel layer and $C_s$ is the correction factor due to the gravel layer. Expressions (1) and (2) are derived from empirical formulations that account for surface materials and the duration of faults, according to IEEE Std 80 [2].

$$V_{tmax} = \left[1000 + 1.5C_s(h_s \cdot K) \cdot \rho_s\right] \cdot \frac{0.116}{\sqrt{t}} \tag{1}$$

$$V_{pmax} = \left[1000 + 6C_s(h_s \cdot K) \cdot \rho_s\right] \cdot \frac{0.116}{\sqrt{t}} \tag{2}$$

In soils with two horizontal stratification layers, the calculation of the electrical potential on the surface becomes more complex. The upper layer, with resistivity $\rho_1$, and the lower layer, with resistivity $\rho_2$, influence the current dispersion and the potential distribution [46]. Waves emitted by the source undergo reflections and refractions, creating an infinite series of source images at different depths, which affects the resulting potential on the surface. The expressions that describe these potentials in stratified soils are adaptations of the expressions for homogeneous soils, with the inclusion of the reflection factor $K$ between layers, as illustrated in Fig. 3(a), in which, $D$ represents the depth of the current source in the soil, $h_1$ is the depth of the first soil layer, $r'_{n+}$, $r'_{n-}$, and $r'_0$ are the distances between the symmetrical image of the point source and point $P$, $r_{n+}$, $r_{n-}$, and $r_0$ are the distances between the point current source and point $P$, $n$ is the summation variable in the range $[1, \infty]$, and $j$ and $k$ are the segments, with $Z_j$ and $Z_k$ representing the depths and $L_j$ and $L_k$ the lengths of segments $j$ and $k$, respectively.

In homogeneous soil, there are no reflection planes, resulting in a reflection factor between layers equal to *zero*. Thus, all terms in the summations in (3) are canceled, except for $n = 0$, where $K^0 = 0^0 = 1$. These analyses are important for the proper design of the grounding grid, ensuring that touch and step potentials remain within safety limits, both in homogeneous and stratified soils. A detailed understanding of the grid parameters and the potentials generated under different soil conditions is necessary to ensure the efficiency and safety of electrical grounding systems [2]. In (3), $R_{jk}$ is the mutual electrical resistance between linear segments, representing the relationship between the voltage induced in the segment $k$ and the dispersion current from the segment $j$, $v_k$ is the potential induced by the dispersion current of the source from the segment $j$ in the segment $k$, $i_j$ is the current in the segment $j$, and $M$ is the solution of the double integral along the lengths $L_j$ and $L_k$. The determination of the function $M$ is based on the studies presented by Campbell [65] and Heppe [39], as given in

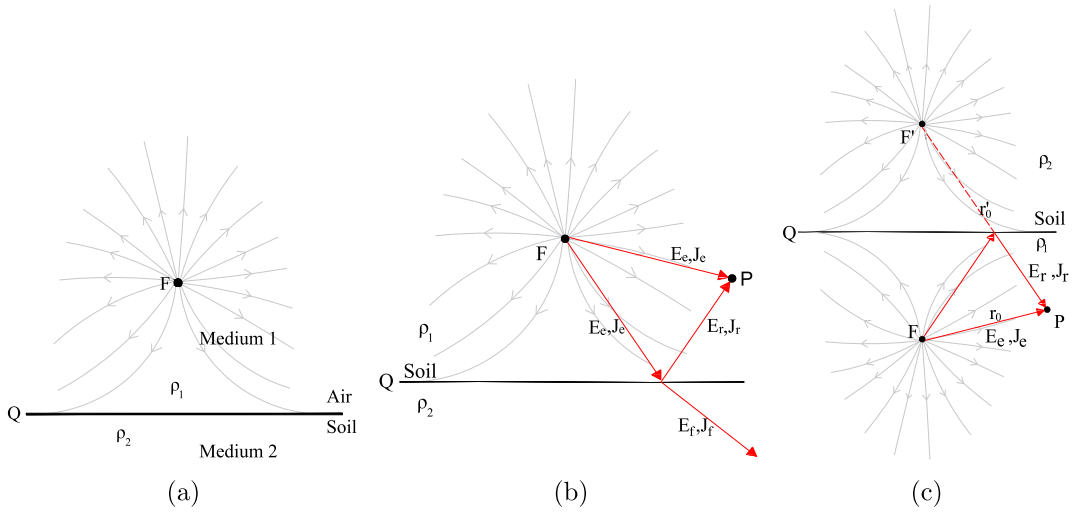


**Fig. 2.** Electrical potential in a homogeneous medium: (a) point current source in a two-layer system, (b) emitted, reflected, and refracted waves, and (c) system for a point in the same medium as the source.

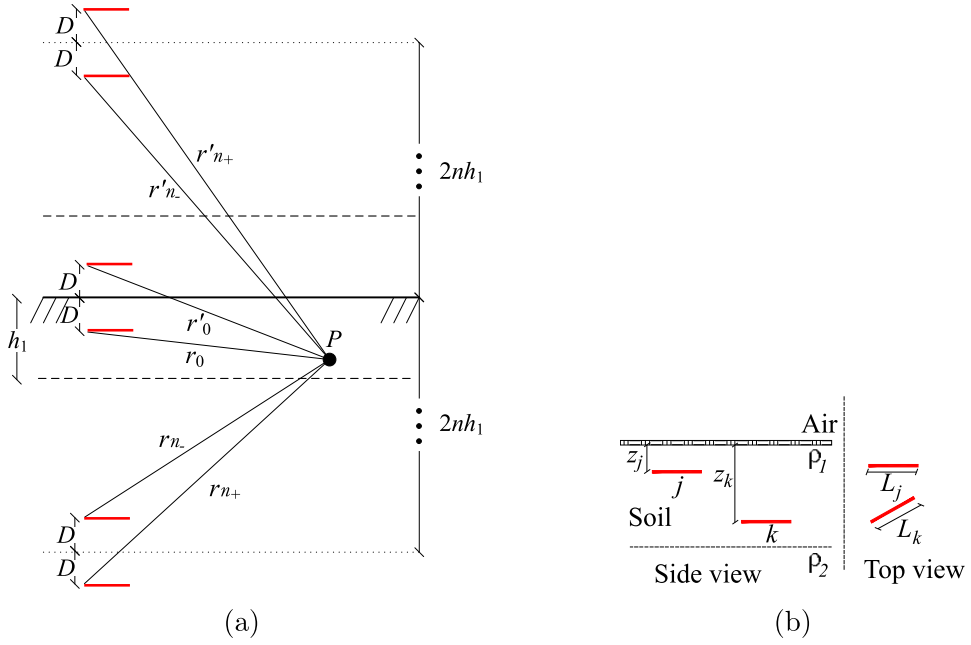


**Fig. 3.** Stratified soil with two layers: (a) reflected images of the source in the first layer of the two-layer stratified soil, and (b) segments in two-layer soil.

(4), where $r$ represents the distance between two infinitesimal length elements along $dL_k$ and $dL_j$.

$$R_{jk} = \frac{v_k}{i_j} = \frac{\rho_1}{4\pi L_k L_j} \left\{ \sum_{n=1}^{\infty} K^n \left[ M(2nh_1) + M(2nh_1 \pm 2D) \right] \right\} \tag{3}$$

$$M = \int \int \frac{1}{r} dL_k dL_j \tag{4}$$

The expressions (3) and (4) extend classical potential formulations to stratified media by incorporating image sources and reflection coefficients, allowing for more accurate modeling of electrical potentials in layered soils.

### 2.4. Mutual and self-resistance calculations in stratified soils

To calculate mutual resistance between two segments buried in the upper layer of stratified soil, the current dispersion of the source segment $j$ and the potential induced in the receiver segment $k$ are considered. The mutual resistance between these segments is determined by integrating the potential along the lengths of both segments, taking into account the reflections and refractions of waves at the interface between the soil layers [46]. Mutual resistance can be expressed in terms of the function $M$, which depends on the distance between the segments and their relative positions in the soil, as illustrated in Fig. 3(b).

When the segments are located in the lower soil layer, the mutual resistance is calculated by considering additional wave reflections at the interface between the layers. In this configuration, the reflection coefficient $K$ is applied to account for the contribution of the images generated at the interface plane and the soil surface, as illustrated in Figs. 4(a) and 4(b). Here, $j'$ represents the image generated by the reflection of $j$ below the interface plane between the two soil layers, $j'_n$ represents the infinite series of images, and $j_n$ are the infinite images. The mutual resistance is again expressed in terms of the function $M$,

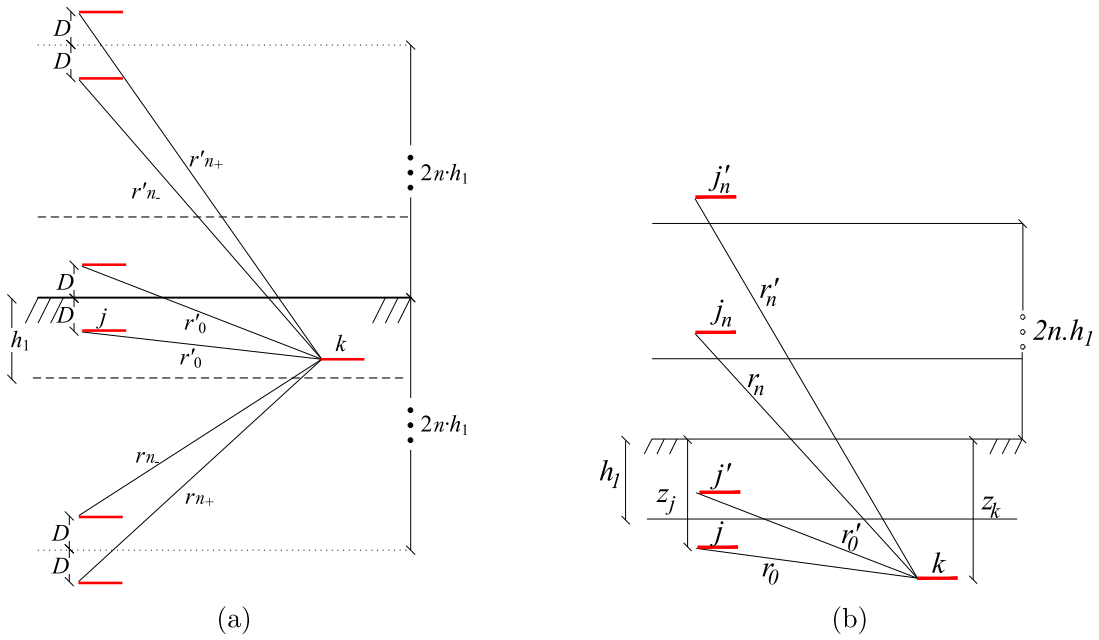


**Fig. 4.** Reflected images between source and receiver segments: (a) in the first soil layer and (b) in the second soil layer.

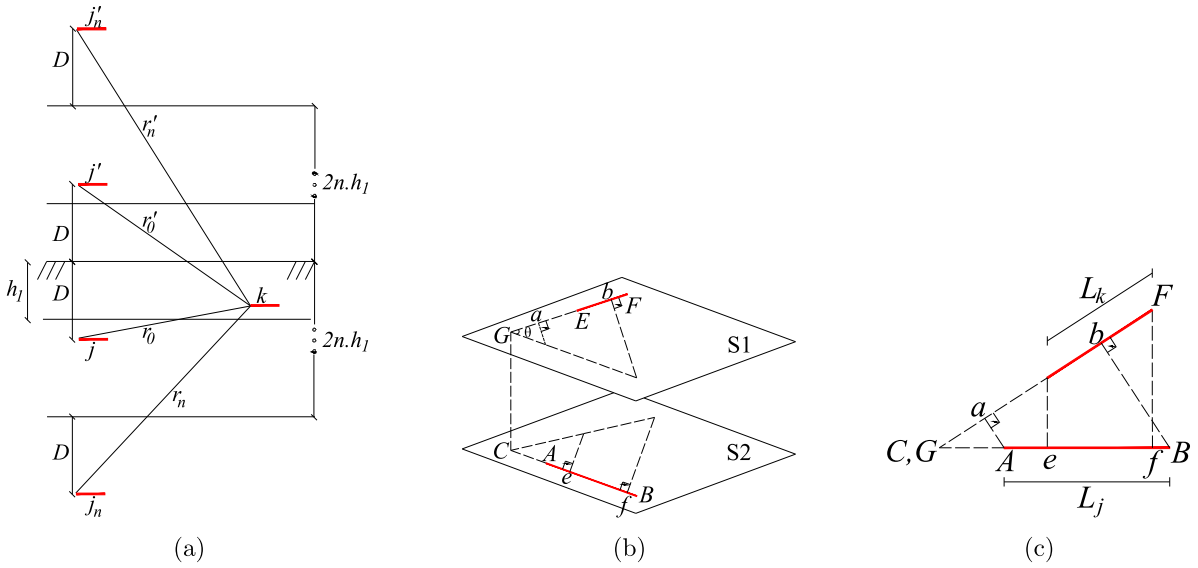


**Fig. 5.** Reflected images with the source in the second layer: (a) receiver segment in the first layer, (b) diagram of the relative position between angled segments, and (c) two-dimensional diagram of the relative position between angled segments.

which is adjusted to reflect changes in reflections and the depth of the buried segments.

In homogeneous soil, the mutual resistance between two segments is simplified, as there are no reflections at the soil interfaces. The mutual resistance is then calculated directly using the function $M$, considering only the distances between the segments and the burial depth [39]. This simplification reduces the complexity of the calculation while still taking into account the potential distribution along the segments, as illustrated in Fig. 5(a), where $r_n$ is the distance between the current source of the point and the point $P$, and $r'_n$ is the distance between the symmetric image of the source of the point and the point $P$.

The self-resistance of a segment is calculated in the same way as mutual resistance, but considering that the segment interacts with itself. To simplify the calculation, an identical segment is placed at a distance equal to the radius of the electrode. This allows the same expressions for mutual resistance to be applied, adjusted for the specific geometric characteristics of the segment [65].

The function $M$ is also used to determine self-resistance, taking into account geometric variables and the relative position between segments, as illustrated in Fig. 5, where $S_1$ and $S_2$ are parallel planes containing the segments, $BC$, $BF$, $BE$, $AF$, $AE$, $FE$, $CG$, and $GF$ are points on the oblique segments $a$, $b$, $e$, and $f$, and $\theta$ is the angle between the oblique segments, with an amplitude ranging from $0 \leq \theta \leq \pi$. Fig. 6 considers the coordinate system $x, y$, both on the ground surface with origin at the current source, and the $z$ axis originating perpendicular to the surface plane, located in Medium 2, composed of air with $\rho_2 = \infty$.

The potential in vertical rods is calculated by applying the concept of electrical potential in stratified soils. The current dissipated along the rod is constant and the potential at a specific point along the rod is determined by integrating over the entire length of the rod and its reflected image in the soil [39]. This calculation yields an expression for

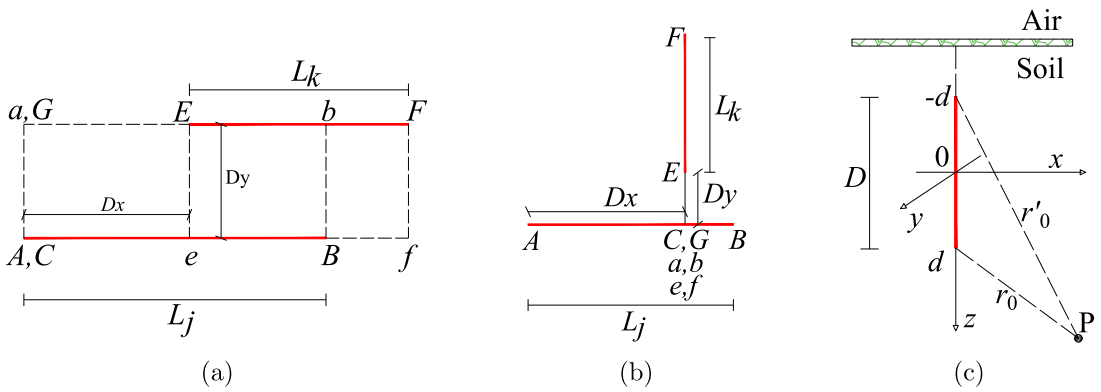


**Fig. 6.** Relative position between segments: (a) parallel, (b) perpendicular and (c) vertical rod in homogeneous soil.

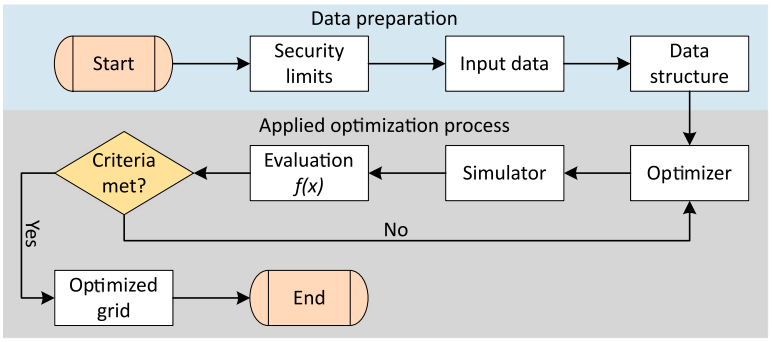


**Fig. 7.** Flowchart of the proposed methodology.

the average potential on the surface of the rod, considering the length of the rod and the resistivity of the soil, as illustrated in Fig. 6(c). In Figs. 6(a) and 6(b), $Dx$ represents the distance between the points $AC$, while $Dy$ denotes the distance between the points $GE$.

## 3. Methodology

This section presents the methodology used to divide the grounding grid into distinct straight segments, with the aim of discretizing the system and enabling the calculation of the dispersion current in each segment. Once the dispersion currents are determined, it will be possible to calculate the voltage at any point on the soil surface. Finally, a methodology will be presented to obtain the optimized geometry of the grounding grid through the optimization process.

### 3.1. Iterative design and segmentation of grounding grids

The design of the electrical grounding grid is typically achieved through an iterative process, starting with an initial grid and adjusting it until the surface potentials, as well as touch and step voltages, are within the safety limits defined by standards. If these requirements are not met, the design is modified until the conditions are satisfied. This work proposes a computational methodology to optimize the grounding grid for any configuration of horizontal conductors and vertical rods to minimize material usage, reduce impedance, and ensure safety. The methodology analyzes the behavior of touch and step potentials in different configurations of conductors and rods. Fig. 7 illustrates the flow of this methodology.

The grounding grid is initially divided into segments, with the following considerations: (i) the current density in each segment is constant throughout its entire length, (ii) each segment has its own dispersion current, (iii) the sum of the dispersion currents in the soil from all segments is equal to the current applied to the grid, and (iv) the potential on the electrode surface that forms the segments is

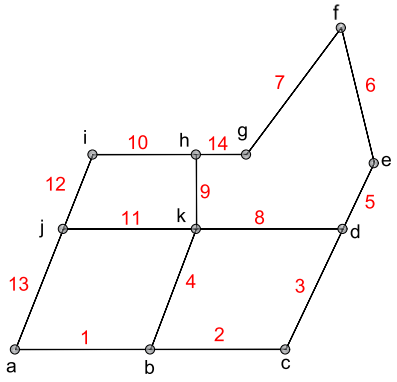


**Fig. 8.** Hypothetical illustration of grounding grid segmentation.

constant and equal to the increase in ground potential (GPR). The grid is appropriately divided into discrete segments at intersection points and changes in the electrode angle. For example, in a grounding grid with the geometry illustrated in Fig. 8, the electrode is divided at intersections $b$, $d$, $h$, $j$, and $k$, as well as at angle changes $a$, $c$, $e$, $f$, $g$, and $i$, resulting in fourteen distinct segments.

The segments are further subdivided into smaller parts, affecting the results, with greater precision achieved as the electrodes are divided into smaller segments. Therefore, the accuracy of the modeling is directly related to the number of segments used, and the ideal model considers an infinite number of segments. Inadequate segmentation typically results in surface potentials higher than the average potential of the electrodes.

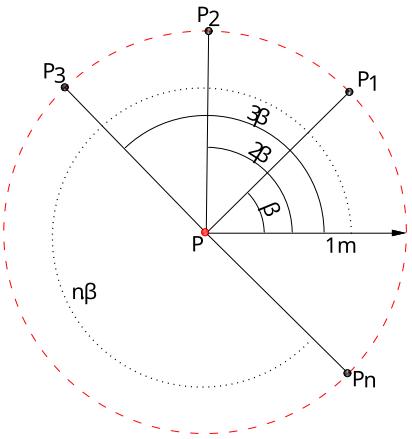


**Fig. 9.** Measurement points for step voltage calculation.

### 3.2. Proposed method for mutual resistance and surface potential calculations

According to (3), the potential induced in segment $k$, shown in Fig. 4(a), by the leakage current from the segment $j$ is obtained by multiplying the mutual electrical resistance between the segments by the dispersion current of the segment $j$. By the superposition theorem, the total potential induced in the segment $k$ is the sum of the potential contributions of all other segments, in addition to the potential induced by the dispersion current of the segment itself, as given by (5), where $n$ is the summation index. In this expression, $m$ is the number of segments in which the electrode is divided, and $V_k$ represents the total potential in the segment $k$. For the system described by (6) to have a solution, it is assumed that the voltages in all segments are equal to the average potential on the electrode, defined as the GPR. The total current injected into the grid, $I_g$, is equal to the sum of the dispersion currents of all segments, as given by (7).

$$\sum_{n=1}^{m} R_{kn} \cdot i_n = V_k \tag{5}$$

$$\begin{bmatrix} R_{11} & R_{12} & R_{13} & \dots & R_{1m} \\ R_{21} & R_{22} & R_{23} & \dots & R_{2m} \\ R_{31} & R_{32} & R_{33} & \dots & R_{3m} \\ \vdots & \vdots & \vdots & \ddots & \vdots \\ R_{m1} & R_{m2} & R_{m3} & \dots & R_{mm} \end{bmatrix} \cdot \begin{bmatrix} i_1 \\ i_2 \\ i_3 \\ \vdots \\ i_m \end{bmatrix} = \begin{bmatrix} V_1 \\ V_2 \\ V_3 \\ \vdots \\ V_m \end{bmatrix} \tag{6}$$

$$I_g = \sum_{n=1}^{m} i_k \tag{7}$$

Thus, the GPR is given by (8), where the GPR becomes a system variable, since the total current injected into the grid, $I_g$, characterized as the short-circuit current, is typically a known parameter of the design, unlike the potential at the electrode. Since the mutual resistance expressions are symmetric $R_{jk} = R_{kj}$, only half of the mutual resistances must be calculated. Knowing the short-circuit current, the system calculates the dispersion currents in each segment and the GPR, allowing the determination of the grounding resistance of the grid.

$$\begin{bmatrix} R_{11} & R_{12} & R_{13} & \dots & R_{1m} & -1 \\ R_{21} & R_{22} & R_{23} & \dots & R_{2m} & -1 \\ R_{31} & R_{32} & R_{33} & \dots & R_{3m} & -1 \\ \vdots & \vdots & \vdots & \ddots & \vdots & -1 \\ R_{m1} & R_{m2} & R_{m3} & \dots & R_{mm} & -1 \\ 1 & 1 & 1 & \dots & 1 & 0 \end{bmatrix} \cdot \begin{bmatrix} i_1 \\ i_2 \\ i_3 \\ \vdots \\ i_m \\ \text{GPR} \end{bmatrix} = \begin{bmatrix} 0 \\ 0 \\ 0 \\ \vdots \\ 0 \\ I_g \end{bmatrix} \tag{8}$$

The surface potential $V_s$ is calculated by summing the potential contributions of each segment at every point on the surface, taking into account the type of soil, the depth of the grid and the thickness of the first layer of soil. Once the surface potential is determined, the touch voltage can be calculated. The step voltage is calculated as the potential difference between a point where the surface potential is measured and an adjacent point, one meter apart, as illustrated in Fig. 9. The coordinates at point $P_n$ are given by:

$$\begin{aligned} x_{Pn} &= x_P + \cos(n \cdot \beta) \\ y_{Pn} &= y_P + \sin(n \cdot \beta) \end{aligned} \tag{9}$$

where $\beta$ is the angle of the step and $1 \leq n \leq \psi$, with $\psi$ being the number of steps required. Expression (9) computes the coordinates of the points used to evaluate the step voltage. The proposed computational process is illustrated in the flow diagram in Fig. 10, which outlines the steps for building the simulator: (i) coordinate transformation and determination of the relative position of segments, (ii) calculation and assembly of the self and mutual resistance matrix, (iii) calculation of the dispersion current in each segment, (iv) calculation of the surface potential and GPR, and (v) calculation of touch and step voltages and the grid resistance.

### 3.3. Coordinate transformations for segment relative positioning

To calculate mutual and self-resistances between segments, it is necessary to know their relative positions and the distances between their points. Changes in the segment coordinates do not affect their relative positions and are applied to reduce the number of expressions and simplify cases of overlap between segments, without altering the results due to this coordinate change. Taking into account two horizontally arranged segments in the soil and using the $x$ and $y$ coordinate system, as illustrated in Fig. 11, the coordinate system is transformed to $x'$ and $y'$ to position the end point of one segment at the origin. The coordinates of the segment endpoints in the $x'$ and $y'$ coordinate system are given by:

$$\begin{aligned} x'_A &= 0 & y'_A &= 0 \\ x'_B &= x_B - x_A & y'_B &= y_B - y_A \\ x'_E &= x_E - x_A & y'_E &= y_E - y_A \\ x'_F &= x_F - x_A & y'_F &= y_F - y_A \end{aligned} \tag{10}$$

By moving the end point of the segment $AB$ to the origin, the transformation is performed in the $u$ and $v$ coordinate systems, positioning the segment $AB$ along the $x$-axis, as illustrated in Fig. 12. The coordinates of the initial and final points of the segments in the system $u$ and $v$ are obtained through a two-dimensional coordinate transformation, given by (11), where $\theta$ represents the inclination of the segment defined by the points $A$ and $B$ relative to the axis $x'$, as given by (12).

$$\begin{aligned} u_A &= 0 & v_A &= 0 \\ u_B &= x'_B \cos(\theta) + y'_B \sin(\theta) & v_B &= -x'_B \sin(\theta) + y'_B \cos(\theta) \\ u_E &= x'_E \cos(\theta) + y'_E \sin(\theta) & v_B &= -x'_E \sin(\theta) + y'_E \cos(\theta) \\ u_F &= x'_F \cos(\theta) + y'_F \sin(\theta) & v_F &= -x'_F \sin(\theta) + y'_F \cos(\theta) \end{aligned} \tag{11}$$

$$\theta = \tan^{-1} \frac{y'_B - y'_A}{x'_B - x'_A} \tag{12}$$

After transformation to the $u, v$ plane, if the segments remain in positions different from those illustrated in Fig. 5, further coordinate transformations are required for the following cases: (i) collinear parallel segments, (ii) non-collinear parallel segments, (iii) perpendicular segments, and (iv) oblique segments. When segment $AB$ is parallel and collinear with segment $EF$, with coordinates in the $u, v$ plane represented by $u_E, u_F < 0$, as illustrated in Fig. 13, the transformation from the $u, v$ plane to the $u', v'$ plane results in (13).

In the case of non-collinear parallel segments, as illustrated in Fig. 14, two situations are considered: (i) $u_E < 0$, and (ii) $v_E, v_F < 0$. For $u_E < 0$, the transformation from the $u, v$ plane to the $u', v'$ plane results in the coordinates given by (14). For $v_E, v_F < 0$, the transformation from the $u, v$ plane to the $u', v'$ plane provides the segment coordinates according to (15).

$$\begin{aligned} u'_E &= u_B - u_F & v'_E &= 0 \\ u'_F &= u_B - u_E & v'_F &= 0 \end{aligned} \tag{13}$$

$$u'_E = u_B - u_F \quad v'_E = v_E$$
$$u'_F = u_B - u_E \quad v'_F = v_F \tag{14}$$

$$u'_E = u_B - u_F \quad v'_E = v_E$$
$$u'_F = u_B - u_E \quad v'_F = v_F \tag{15}$$

When segments $AB$ and $EF$ are perpendicular, as illustrated in Fig. 15, two situations are possible: (i) $u_E, u_F < u_A$ and (ii) $v_E, v_F < 0$. In the first situation, where $u_E, u_F < u_A$, the coordinates of the segment $EF$ after transforming from the $u, v$ plane to the $u', v'$ plane are given by (16). In the second situation, with $v_E$ and $v_F < 0$, the transformation from the $u, v$ plane to the $u', v'$ plane results in the coordinates of the segment $EF$ given by (17). In the case of the oblique segments $AB$ and $EF$, as illustrated in Fig. 16, there are also two situations: (i) $v_E$ and $v_F < 0$ and (ii) $u_F < u_E$. For the condition where $v_E, v_F < 0$, the coordinates of the segment $EF$ after the transformation from the $u, v$ plane to the $u', v'$ plane are given by (18). For condition $u_F < u_E$, the coordinates of the segment $EF$ in the new coordinate system are given by (19).

$$u'_E = u_B - u_E \quad v'_E = v_E$$
$$u'_F = u_B - u_F \quad v'_F = v_F \tag{16}$$

$$u'_E = u_E \quad v'_E = \mid v_E \mid$$
$$u'_F = u_F \quad v'_F = \mid v_F \mid \tag{17}$$

$$u'_E = u_E \quad v'_E = \mid v_E \mid$$
$$u'_F = u_F \quad v'_F = \mid v_F \mid \tag{18}$$

$$u'_E = u_B - u_F \quad v'_E = \mid v_F \mid$$
$$u'_F = u_B - u_E \quad v'_F = \mid v_E \mid \tag{19}$$

After the coordinate transformations, the relative positions of the segments are checked to adjust them appropriately, enabling the calculation of the distances between them. Next, a matrix is constructed that contains the $x$ and $y$ coordinates of the initial and final positions of each segment, as well as the vertices of the perimeter of the area where the grounding grid is or will be installed. The expressions (10) to (19) define two-dimensional transformations used to reposition grid segments within local coordinate systems, thus simplifying the calculation of mutual and self-resistances. These transformations are based on classical approaches in geometric modeling.

### 3.4. Proposed optimization algorithm

For the execution of calculation routines in the simulator, the following input data are used: (i) soil resistivity of the first layer [Ωm], (ii) soil resistivity of the second layer [Ωm], (iii) thickness of the first soil layer [m], (iv) current applied to the grid [A], (v) conductor radius used in the grid [m], (vi) structure containing matrices with segment coordinates, (vii) grounding grid depth [m], (viii) diameter of the vertical rod [in], (ix) length of the vertical rod [m], (x) angle for step voltage calculation $\psi$ [°], (xi) maximum segment length [m], and (xii) step size for potential and voltage calculations [m]. The simulator outputs values for surface voltage, GPR, touch voltage, step voltage, and grounding grid resistance, which are subsequently used in the optimization process.

The optimization process of the electrical grounding grid aims to improve the performance of matrices of varying sizes [66] the system performance in terms of horizontal electrode geometry, potential uniformity, vertical rod placement and cost reduction in construction [67]. Some studies use numerical methods based on finite elements and heuristics such as genetic algorithms and Particle Swarm Optimization (PSO) to determine the optimal spacing between horizontal electrodes, making the grounding system more efficient and minimizing electrical resistance, as well as step and touch voltages. The optimization algorithm proposed in this work is based on an adaptive evolutionary algorithm which focuses on the population level and population diversity.

The proposed methodology utilizes advanced mathematical modeling and computational algorithms to dynamically optimize grounding grids, making it suitable for integration into real-time industrial control systems. Evolutionary algorithms enable automated systems to fine-tune grounding configurations in response to changing soil conditions and fault scenarios, making this approach particularly advantageous for automated substations and distributed control systems (DCS) in complex industrial environments. The workflow of the optimization algorithm is shown in Fig. 17.

The input data for the algorithm includes: (i) initial grid design in Drawing Exchange Format `*.dxf`, (ii) gravel resistivity [Ωm], (iii) gravel layer thickness [m], (iv) number of possible solutions per generation, (v) population size, (vi) use or non-use of vertical rods in the optimization process, (vii) number of generations, (viii) protection operation time in seconds, and (ix) weights for the evaluation function. The maximum admissible step and touch voltages are given by (1) and (2). The initial population is formed on the basis of the coordinate matrices of the horizontal segments and, if present, the vertical rods in the initial grid. Fig. 18 illustrates the matrix with the initial grid, entered into the simulator in `*.dxf` format, from which the first individuals of the population are generated.

The initial population individuals are generated by removing and/or adding new segments, using the coordinates in the initial coordinate matrix as a reference. Fig. 19 illustrates the formation of two individuals from the initial grid. Individual 1 is formed by removing the segments $h_1$, $n_1$, $e_1$, $j_1$, $f_1$, and $i_1$ from the initial grid, while Individual 2 is created by adding the segments $a_2$, $b_2$, $c_2$, and $d_2$ to the initial grid. In the proposed algorithm, the first five individuals formed, along with the initial grid, are selected as parents to generate various new individuals in the population.

Each new individual in the population is created from two parents, randomly selected from the first five individuals and the initial matrix. The new individual is composed of segments inherited from both parents, with the possibility of new segments being created due to the intersection of inherited segments. Fig. 20 illustrates the crossover and

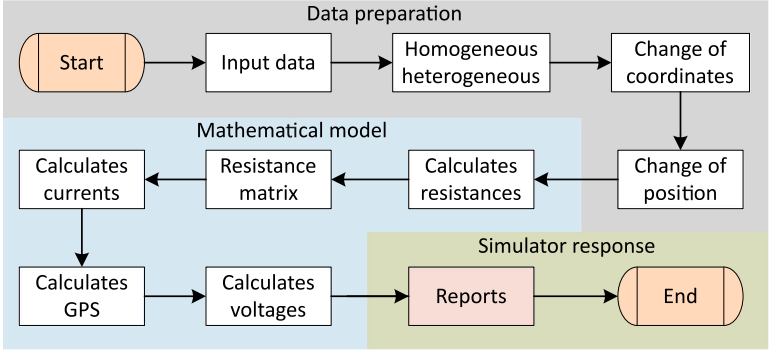


**Fig. 10.** Flowchart of the proposed simulator.

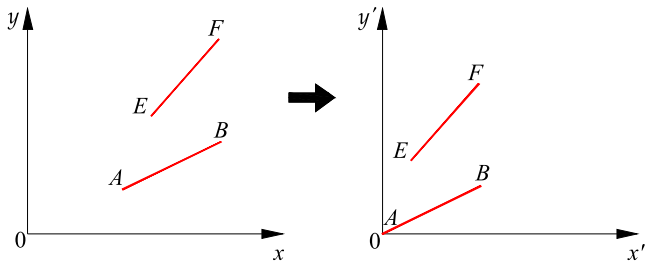


**Fig. 11.** Illustration of the $x \times y$ and $x' \times y'$ coordinate systems.

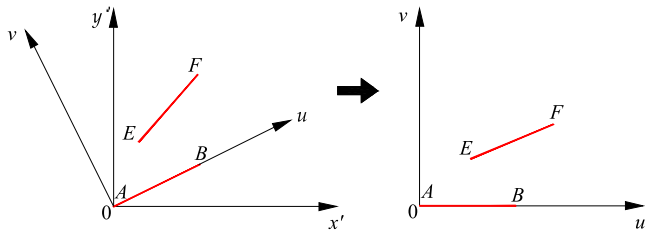


**Fig. 12.** Illustration of the $x' \times y'$ and $u \times v$ coordinate systems.

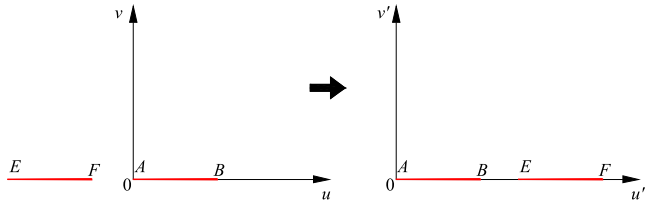


**Fig. 13.** Illustration of the system with collinear parallel segments.

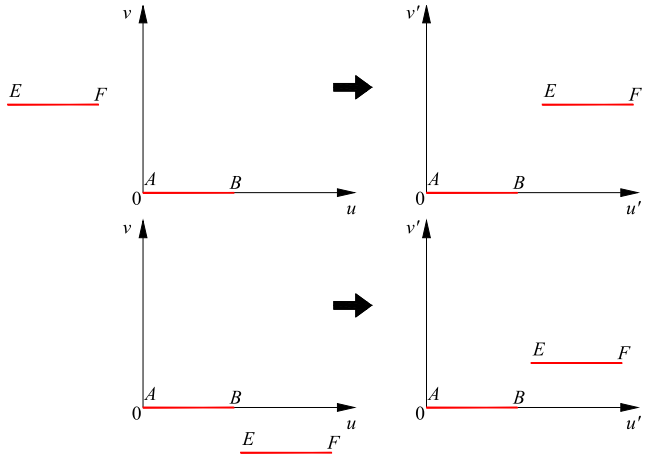


**Fig. 14.** Illustration of the system with non-collinear parallel segments.

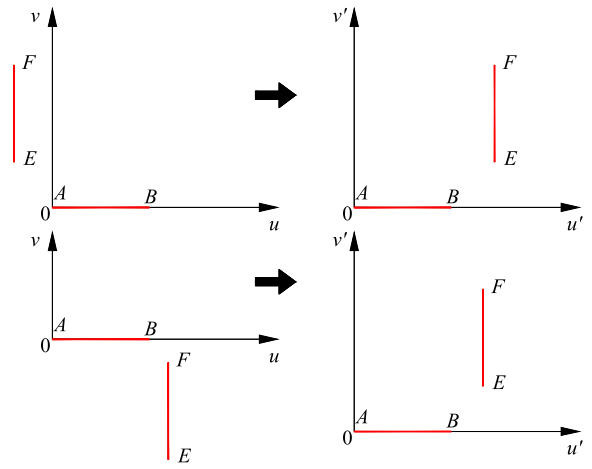


**Fig. 15.** Illustration of the system with perpendicular segments.

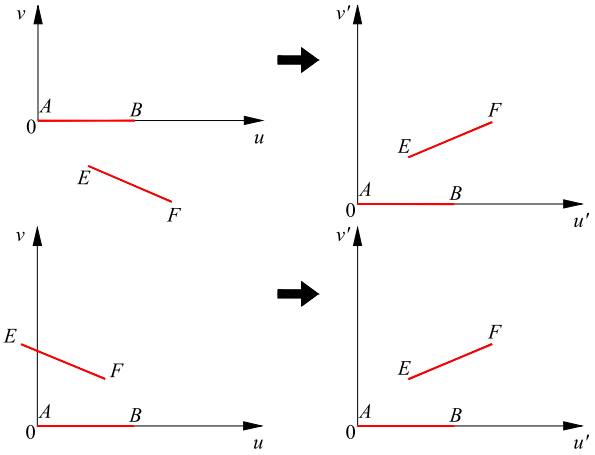


**Fig. 16.** Illustration of the system with oblique segments.

mutation process between parents. In the example, Individual A inherits segments $a_1$, $b_1$, $c_1$, $h_1$, $d_1$ and $i_1$ from Parent 1, and segments $c_2$, $e_2$, $f_2$ and $g_2$ from Parent 2. The intersection of the segments $i_1$ and $f_2$ results in the creation of four new segments: $a_3$, $b_3$, $c_3$ and $d_3$. Furthermore, individuals can acquire segments without intersection with inherited segments, as in the case of Individual B in Fig. 20, which receives segments $a_4$, $b_4$, $c_4$, $d_4$, $e_4$, and $f_4$ by mutation.

Fig. 21 illustrates the formation of the population in a given generation $g_i$, with $i = 1, 2, \ldots, g_{max}$. The population consists of a set of matrices of varying sizes, as the number of rows in each matrix depends on the number of segments each individual in the population has. Although heuristic optimization techniques, such as genetic algorithms, typically form the population with individuals of uniform size and a single matrix per generation, the proposed algorithm uses a set of matrices per generation, resulting in a three-dimensional population matrix.

After the population is formed, it is necessary to process the segments of each individual's matrix, as some individuals may have vertices outside the perimeter of the area designated for the construction of the electrical grounding grid. The processing involves checking all segments and, upon identifying vertices outside the area limits, cutting the respective vertex and creating a new vertex at the perimeter boundary of the construction area. Fig. 22 illustrates a situation in which the grid has a segment outside the defined perimeter. The segment $u_1$, shown in red, extends beyond the limits of the grid area. During processing, the algorithm removes the segment $u_1$ portion that is outside the limits, generating segments $k_1$ and $m_1$. After processing the segments and building the matrix with the vertex coordinates, the algorithm creates the vertical rod matrix. The coordinates of this matrix are defined on the basis of the vertices of the horizontal segment matrix. Initially, the selection of vertices for vertical rods is performed randomly. With the horizontal segment and vertical rod matrices properly adjusted, the next step is simulation.

After the simulation, the evaluation phase of the individuals in the created population takes place. This process uses a specific evaluation function that assesses the performance of individuals concerning: (i) grid length, (ii) step voltage, (iii) touch voltage, (iv) grid resistance,

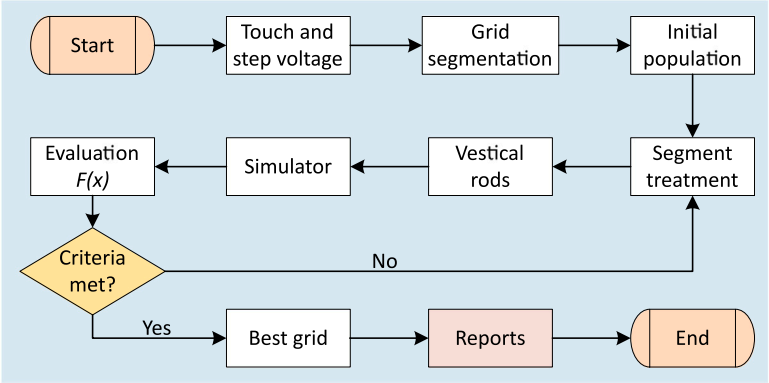


**Fig. 17.** Flowchart of the applied optimization process.

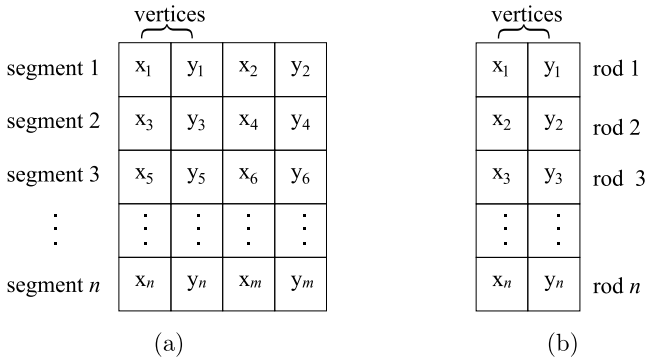


**Fig. 18.** Illustration of the two-dimensional matrix with the coordinate formation of a population individual: (a) horizontal segments and (b) vertical rods.

and (v) number of vertical rods. The evaluation function for the proposed algorithm is expressed by (20), where $\gamma$ represents the penalty cost for the individual, associated with the constraint applied when the GPR exceeds the maximum surface potential. $V_s$ is the surface potential, $P_i$ is the weight vector and $T_i$ corresponds to the normalized value of the length of the grid, step voltage, touch voltage, resistance to the grid, and the number of vertical rods.

$$\min f(x) = \begin{cases} \sum_{i=1}^{n} P_i \cdot T_i & \texttt{if} \quad V_s \leq \text{GPR} \\ \sum_{i=1}^{n} P_i \cdot T_i + \gamma & \texttt{if} \quad V_s > \text{GPR} \end{cases} \tag{20}$$

Subject to:

$$V_t \leq V_{t,\max} \tag{21}$$

$$V_p \leq V_{p,\max} \tag{22}$$

$$R_g \leq R_{g,\max} \tag{23}$$

$$L \leq L_{\max} \tag{24}$$

The expression (20) defines the objective function of the optimization algorithm, where $P_i$ are the weights assigned to the technical criteria, that is, step voltage, touch voltage, grounding resistance, and total length of the grid, and $T_i$ are their corresponding normalized values. A penalty term $\gamma$ is introduced when the surface potential $V_s$ exceeds the increase in the reference ground potential (GPR), forcing the algorithm to discard physically infeasible solutions. Expressions (21) to (24) define the maximum permissible limits for $V_{t,\max}$, $V_{p,\max}$, $R_{g,\max}$, and $L_{\max}$, as established by IEEE Std 80 [2]. In this context, $V_t$ and $V_p$ represent step and touch voltages, respectively, $L$ is the total length of the grounding grid and $R_g$ is the resistance to grounding.

The terms $V_{t,max}, V_{p,max}, R_{g,max}, L_{max}$ denote the maximum values allowed by the regulatory standards, while the constraint $V_s \leq GPR$ is embedded within the objective function. In Eq. (20), the parameter $\gamma$ is introduced to ensure that the optimization algorithm does not consider physically infeasible solutions. Specifically, when the condition $V_s >$ GPR occurs, the model applies a significant penalty to the evaluation function, guiding the search for viable configurations. Mathematically, this penalty is represented by (25), where $M$ is a sufficiently large value used to discard solutions that violate this constraint. Although $M$ does not need to be fixed, it must be high enough to ensure that infeasible individuals receive a worse evaluation than any physically plausible solution.

$$\gamma = \begin{cases} 0, & \texttt{if} \quad V_s \leq \text{GPR} \\ M, & \texttt{if} \quad V_s > \text{GPR} \end{cases} \tag{25}$$

The inclusion of this penalty ensures that the optimization process prioritizes grounding grid geometries that comply with the physical constraints of the problem, preventing configurations that would be impractical for real-world implementation. In Eq. (20), $T_i$ is defined by Eq. (26), where $T$ represents the computed value for these parameters, and $T_{max}$ denotes the maximum allowable value for each.

$$T_i = \frac{T}{T_{max}} \tag{26}$$

The expression (25) introduces a penalty term $M$ whenever a solution violates the surface potential limit, thus preventing the selection of infeasible individuals. Expression (26) performs the normalization of the technical criteria, where $T_{\max}$ is the reference value defined based on the initial grid or established by technical standards [2]. The maximum length of the grid is taken as the value calculated from the initial grid, and the maximum number of vertical rods is defined as the total number of vertices in the initial grid. The maximum values for step voltage, touch voltage, and grounding resistance are established by standards such as the GSSG-IEEE standard [2]. After evaluating the individuals, the algorithm checks if the stopping criteria have been met. For the proposed algorithm, the stopping criteria are: (i) the number of generations or (ii) the value of the evaluation function. If one of the stopping criteria is met, the algorithm ends its process and presents the best individual along with its respective parameters.

Algorithm 1 outlines the steps involved in optimizing the grounding grid, beginning with the definition of parameters such as grid dimensions, vertical rod distribution (initial estimation based on prior knowledge from the designer), and regulatory criteria for step voltage, touch voltage, and resistance. A maximum number of iterations is set to ensure convergence, terminating the process when the objective function reaches an acceptable value or the iteration limit is met. The parameter configuration accounts for geometric constraints and

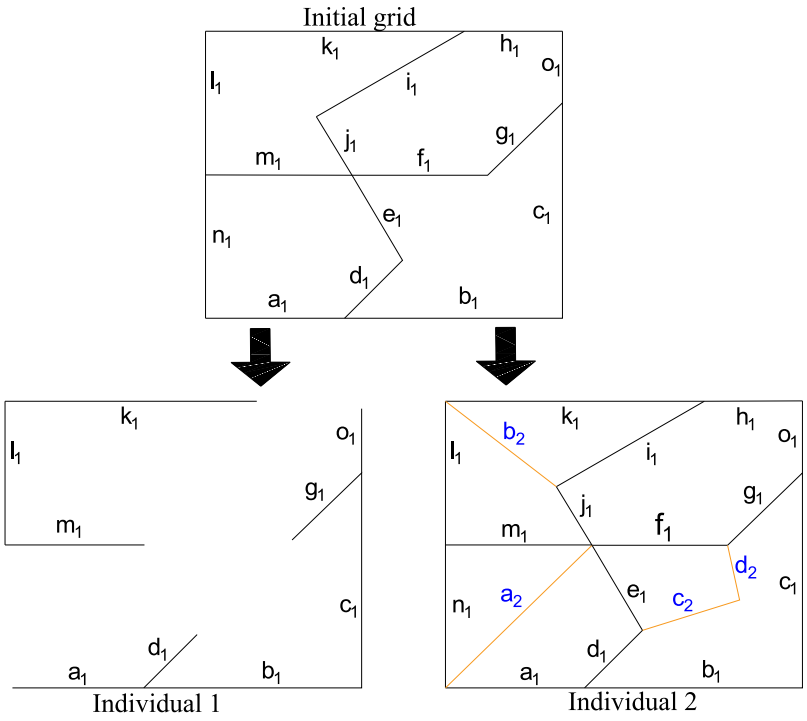


**Fig. 19.** Illustration of the creation of new individuals from the initial matrix.

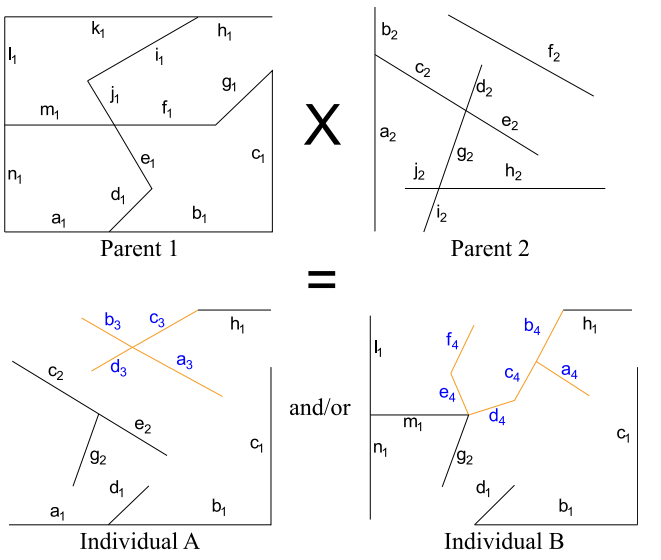


**Fig. 20.** Illustration of the new population creation through the crossover and mutation process.

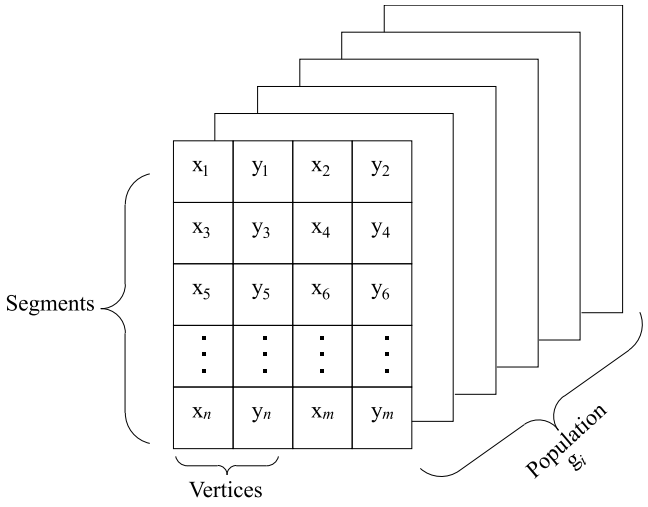


**Fig. 21.** Illustration of the creation of the three-dimensional matrix forming the population of a given generation.

soil properties, where electrical resistivity varies with depth and seasonal conditions, ensuring greater accuracy in modeling and structural adjustments to the grid. The data preprocessing stage includes variable normalization and the removal of inconsistencies, ensuring the reliability of field measurements. Variations in soil electrical resistivity are incorporated to allow dynamic adjustments during algorithm execution.

## 4. Results

This section presents the results obtained from the application of the proposed methodology through five case studies aimed at validating the developed method. In Case study 1 and Case study 2, the optimization algorithm's behavior is analyzed concerning the influence of apparent soil resistivity and the depth of the electrical grounding grid, considering the length of the grid. In Case study 3, Case study 4, and Case study 5, optimized grounding grid geometries are presented, with comparisons to grounding grids obtained through traditional methods.

### 4.1. Validation of the simulator with literature data

To validate the proposed simulator, the results of studies in the literature were used and compared with those obtained from the simulator using the same input parameters. Comparisons include values for grounding resistance, touch voltage, and step voltage in grounding grids for homogeneous and heterogeneous soils. For electrical resistance, the simulator results were compared with those specified in

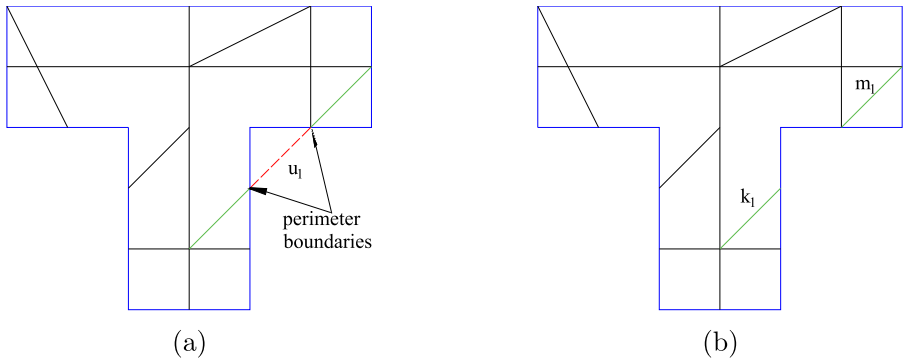


**Fig. 22.** Illustration of grid creation: (a) with a segment extending beyond the area limits and (b) with adjusted segments.

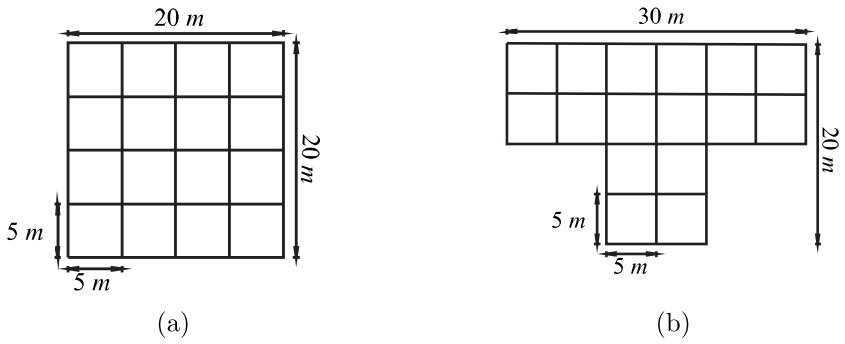


**Fig. 23.** Conventional grids used to validate the simulator's resistance calculations with geometry: (a) square and (b) T-shaped.

**Algorithm 1** Optimization Procedure for Grounding Grid

**Input:** Initial grounding grid parameters, maximum number of iterations $N_{\max}$, tolerance $\epsilon$
**Output:** Optimized grounding grid configuration
Initialize the grid with initial parameters
Define an evaluation function based on impedance minimization and safety constraints
Set penalty functions to prevent physically unfeasible configurations
Define convergence criteria based on the number of iterations and solution stability
$n \leftarrow 0$
**while** $n < N_{\max}$ **and** convergence criteria not met **do**
    Generate a new grid configuration by applying variations to parameters
    Compute the equivalent impedance and check safety criteria
    Apply penalties if constraints are not met
    Evaluate the objective function for the new configuration
    **if** new configuration improves the objective function **then**
        Update the current solution
    **end if**
    $n \leftarrow n + 1$
**end while**
Return the optimized grounding grid configuration

the GSSG-IEEE standard [2], considering square grids and geometry T-shaped. Each grid was divided into 16 square subgrids, with a distance 5 m between the parallel electrodes, as illustrated in Fig. 23. In the calculations, the grids were segmented into 5 m parts, with a depth of 0.5 m, a conductor radius of 0.005 m, and an apparent soil resistivity of $\rho_a = 100$ Ωm.

Table 1 presents the grounding resistance values of the grids illustrated in Fig. 23, considering homogeneous soil. These values were calculated using the simplified expressions mentioned in the GSSG-IEEE standard [2] and the boundary element method (BEM) developed by Ghoneim [68]. The GSSG-IEEE standard [2] does not specify which method is superior, so, by convention, the proposed simulator was used as a reference. The percentage value in Table 1 indicates the difference between the value obtained by the proposed simulator and the other methods. The values found by the proposed method are observed to be similar to those obtained by the average potential method described by Dwight [36] for the grounding grid T. For the square grid, the results of the proposed method are close to those obtained by the boundary element method described by Ghoneim [68].

To compare the step and touch voltage values obtained from the proposed simulator with those derived using the simplified expressions provided by the GSSG-IEEE standard [2], three grounding grid geometries were analyzed: a rectangular grid of 35 m × 20 m with subgrids 28, a L-shaped grid of 30 m × 20 m with subgrids 16, and a T-shaped grid of 30 m × 25 m with subgrids 18, as illustrated in Fig. 24. The comparison was carried out for homogeneous and heterogeneous soils. For each geometry, the grid was divided into 16 square sub-grids with 5 m spacing between parallel conductors, a depth of 0.5 m, a conductor radius of 0.005 m, a grid current of 1000 A, a step voltage angle of $\psi = 90°$, and a simulation step of 1 m.

For homogeneous soil, a resistivity of 300 Ωm was assumed. The depth of the first soil layer was set to an arbitrary value, as the expressions used are invariant with respect to this parameter. Table 2 and Table 3 present the values for the maximum step voltage and the maximum touch voltage, respectively, obtained using the conventional method and the proposed simulator for homogeneous soil. The percentage difference was calculated as the absolute difference between the values obtained from the GSSG-IEEE [2] standard and those found using the proposed method.

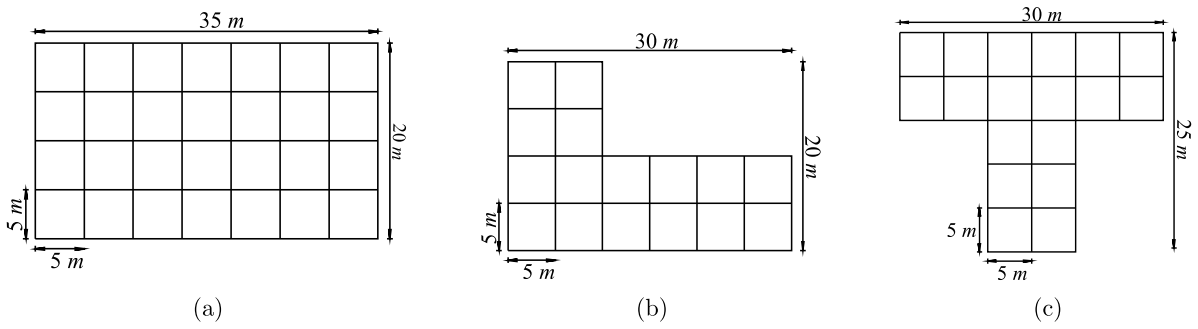


**Fig. 24.** Conventional grounding grids with geometries: (a) square, (b) L-shaped and (c) T-shaped.

**Table 1**
Comparison between the proposed method and other methods from the literature.

| Method | Grid | |
|---|---|---|
| | Square | T |
| Laurent | 3.049 Ω<br>15.7% | 2.985 Ω<br>10.3% |
| Dwight | 2.216 Ω<br>6.4% | 2.216 Ω<br>1.0% |
| Schwarz | 2.604 Ω<br>10.0% | 2.542 Ω<br>13.6% |
| Sverak | 2.624 Ω<br>10.8% | 2.600 Ω<br>16.2% |
| Nahman | 3.149 Ω<br>33.0% | –<br>– |
| Chow | 3.262 Ω<br>37.8% | –<br>– |
| MEC | 2.363 Ω<br>0.2% | –<br>– |
| Proposed simulator | 2.367 Ω | 2.238 Ω |

**Table 2**
Step voltage in homogeneous soil.

| Geometry | IEE Std. 80 [V] | Proposed simulator [V] | Difference [%] |
|---|---|---|---|
| Rectangular | 814.47 | 737.18 | 10.48 |
| L-shaped | 1228.98 | 930.61 | 32.06 |
| T-shaped | 1010.44 | 937.59 | 7.77 |

**Table 3**
Touch voltage in homogeneous soil.

| Geometry | IEE Std. 80 [V] | Proposed simulator [V] | Difference [%] |
|---|---|---|---|
| Rectangular | 1207.85 | 1219.54 | 0.96 |
| L-shaped | 1848.63 | 1554.25 | 18.94 |
| T-shaped | 1554.54 | 1560.96 | 0.41 |

In the analysis of heterogeneous soils with stratification into two horizontal layers, the electrical resistivity of the first layer is considered 200 Ωm, the thickness of the first layer is 6 m, and the electrical resistivity of the second layer is 400 Ωm. Since the conventional method of the GSSG-IEEE standard [2] assumes homogeneous soil, it was necessary to calculate the equivalent apparent resistivity of stratified soil using the method proposed by Endrenyi [69], which assumes homogeneous soil. This method takes into account certain geometric characteristics of the grounding grid, allowing the calculation of the apparent resistivity for each grid, resulting in: (i) 266.67 Ωm for the rectangular grid, (ii) 261.69 Ωm for the L-shaped grid, and (iii) 264.76 Ωm for the grid T-shaped.

**Table 4**
Step voltage in heterogeneous soil.

| Geometry | IEE Std. 80 [V] | Proposed simulator [V] | Difference [%] |
|---|---|---|---|
| Rectangular | 723.98 | 556.02 | 30.21 |
| L-shaped | 1072.90 | 689.38 | 55.63 |
| T-shaped | 891.75 | 693.81 | 28.53 |

**Table 5**
Touch voltage in heterogeneous soil.

| Geometry | IEE Std. 80 [V] | Proposed simulator [V] | Difference [%] |
|---|---|---|---|
| Rectangular | 1.073.66 | 901.77 | 19.06 |
| L-shaped | 1613.85 | 1131.02 | 42.69 |
| T-shaped | 1371.94 | 1133.86 | 21.00 |

Tables 4 and 5 present the values obtained for the maximum step voltage and the maximum touch voltage, respectively, on heterogeneous soil, using both the conventional method and the proposed simulator. It is observed that the largest discrepancies occurred in the touch voltage and step voltage for the L-shaped grid. The method suggested by the GSSG-IEEE standard [2] is based on simplified expressions developed for square grids, applying correction factors for other geometries. These correction factors can introduce errors, which vary depending on the area and length of the grid electrodes.

### 4.2. Application of the optimization process

The optimization algorithm used, although inspired by genetic algorithms, exhibits significant differences in its methodology, particularly in the formation of individuals. Unlike traditional genetic algorithms, which use fixed-size chromosomes resulting in matrices of consistent dimensions across generations, the proposed optimization algorithm utilizes individuals with chromosomes of varying sizes, producing three-dimensional matrices for each generation. The algorithm features fixed crossover and mutation rates, with the number of generations also being fixed and serving as the stopping criterion. Furthermore, the application of the optimization algorithm requires soil stratification, if more than two layers are present, they must be reduced to two layers.

In some cases, it is necessary to use ladder network theory to determine the equivalent impedance, and thereby calculate the current applied to the grid. The optimization algorithm identifies the most suitable individual that meets the safety criteria for electrical grounding grides, considering the touch voltage, step voltage, and the grid's lowest resistance. The proposed algorithm employs: (i) ten individuals per generation, (ii) a linear crossover rate of 50%, (iii) a mutation rate of 0.2%, and (iv) a stopping criterion of 30 generations or $f(x)_{min} = 0$. The evaluation function in (20) is formulated based on the length of the grid, the touch voltage, the step voltage, the resistance of the grid, and the number of vertical rods. All simulations were conducted on an

**Table 6**
Grid length × soil resistivity for Case study 1.

| Resistivity $\rho_a$ [Ωm] | Length [m] |
|---|---|
| 100 | 87 |
| 150 | 90 |
| 200 | 92 |
| 250 | 98 |
| 300 | 103 |
| 350 | 105 |
| 400 | 107 |
| 450 | 108 |
| 500 | 108.5 |
| 550 | 108.8 |
| 600 | 109.2 |
| 650 | 111 |
| 700 | 116 |
| 800 | 125 |
| 900 | 136 |
| 1000 | 148 |

**Table 7**
Grid length × grid depth for Case study 2.

| Mesh depth [m] | Length [m] |
|---|---|
| 0.5 | 98.5 |
| 0.6 | 97.1 |
| 0.7 | 95.5 |
| 0.8 | 91.2 |
| 0.9 | 88.1 |
| 1.0 | 84.6 |
| 1.2 | 84.2 |
| 1.3 | 83.8 |
| 1.4 | 84.4 |
| 1.5 | 84.9 |
| 1.7 | 85.3 |
| 1.8 | 85.8 |
| 2.0 | 86.6 |
| 2.1 | 86.4 |
| 2.3 | 85.8 |
| 2.5 | 84.3 |

Intel i5-3230M computer with a 2.6 GHz CPU and 6 GB of DDR3 1600 MHz RAM.

To perform the case study calculations, the following input data are required: (i) perimeter design of the area in Drawing Exchange Format `*.dxf`, (ii) depth of the grounding grid [$m$], (iii) cross-sectional area of the horizontal electrode [mm$^2$], (iv) resistivity of the first soil layer [$\Omega m$], (v) resistivity of the second soil layer [$\Omega m$], (vi) depth of the first layer [$m$], (vii) current applied to the grid [$A$], (viii) maximum segment length [$m$], (ix) step size for potential and voltage calculations [$m$], (x) angle $\psi$ step for step voltage calculation [°], (xi) number of generations, (xii) number of individuals per generation, (xiii) use of vertical rods, and (xiv) weights $P_i$ of the evaluation function variables $f(x)_{min}$.

### 4.3. Case study 1: influence of soil resistivity on grounding grid length

To demonstrate the behavior of the proposed optimization algorithm, this case study analyzes the influence of apparent soil resistivity on the length of the grounding grid. The study considered a 10 m×10 m area, with a grid current of 350 A, a grid depth of 0.6 m, a horizontal conductor with a cross-sectional area of 35 mm$^2$, and a gravel resistivity of 3000 Ωm. Table 6 presents the average values of grid length obtained after ten simulations for different apparent soil resistivities. Fig. 25 shows the relationship between the apparent resistivity of the soil and the increase in the conductors, with the goal of keeping the grounding grid within the limits established by the standards. Vertical rods were not considered in this case study.

As soil resistivity increases, the algorithm adds horizontal conductors to maintain grounding resistance, step voltage, and touch voltage within regulatory limits. Table 6 shows that as resistivity ranges from 100 Ωm to 1000 Ωm, the length of the grid increases from 87 m to 148 m, indicating a nearly linear relationship. This increase becomes more pronounced beyond 700 Ωm, suggesting that soils with high resistivity require additional conductors to ensure system safety.

The increase in the length of the grid as a function of the resistivity of the soil is found to be relatively linear up to 700 Ωm. Beyond this point, growth becomes more pronounced, with a significant increase of approximately 30 m between 800 Ωm and 1000 Ωm. This suggests that, for soils with resistivity greater than 700 Ωm, the addition of horizontal conductors becomes less efficient, indicating the need to consider alternative strategies, such as incorporating vertical rods or using materials with lower resistivity, to optimize the grounding system.

### 4.4. Case study 2: influence of depth

This case study evaluates the influence of the depth of the grounding grid on its length. An area of 10 m×10 m was used, with a grid current of 350 A, and heterogeneous soil with resistivities of 200 Ωm and 100 Ωm for the first and second layers, respectively. The thickness of the first soil layer was 1.3 m, with a horizontal cross-sectional area conductor 35 mm$^2$ and a gravel resistivity of 3000 Ωm. Vertical rods were not considered in this case study.

Table 7 shows the average length of the grounding grid after ten simulations conducted for different depths of the grounding grid. Fig. 26 illustrates the relationship between the depth of the grounding grid and the reduction in conductors, with the goal of maintaining the grid within the standards established by the regulations. It is observed that as the depth of the grid increases, the algorithm responds by reducing the number of horizontal conductors. This occurs because an increase in the depth of the grid approaches the second soil layer, which has a lower resistivity, resulting in a decrease in the length of the horizontal conductors.

Based on the values in Table 7, it is observed that the length of the grid decreases linearly as the depth of the grid increases from 0.5 m to 1.3 m, reaching a minimum value of 83.8 m at this depth. However, beyond 1.4 m, the length of the grid begins to increase again, indicating a possible limitation in the effect of depth on the reduction of horizontal conductors. This behavior suggests that, after a certain depth, the influence of the second soil layer, with lower resistivity, becomes less significant, which may indicate a saturation point in the benefit gained from increasing the grid depth. This reversal in the trend of reducing the length of the grid highlights the need for a more detailed analysis to identify the optimal depth, considering the balance between grid efficiency and the additional installation costs at greater depths.

### 4.5. Case study 3: optimization of grounding grid for extensive perimeter area

In this case study, an area with a perimeter of 40 m × 50 m was considered, using a horizontal conductor with a cross section of 35 mm$^2$ and a grounding grid depth of 0.8 m. The resistivity of the upper layer was 500 Ωm and that of the second layer was 80 Ωm, with a thickness of 6 m for the upper layer. The current in the grid was 1000 A, the resistivity of the gravel was 3000 Ωm, and the thickness of the gravel layer was 0.2 m. The protection activation time was 0.5 s, and an angle of $\psi = 5°$ was used for the step voltage calculation. Table 8 presents the values obtained using the GSSG-IEEE [2] method and the proposed optimization method. The step and touch voltages obtained are within the limits established by the standards, with 2273.829 V for the step voltage and 691.494 V for the touch voltage.

Fig. 27 shows the grid obtained by the optimization algorithm, with red circles indicating the locations of the vertical rods. Figs. 28(a) and 28(b) show the surface potential within the perimeter of the grounding

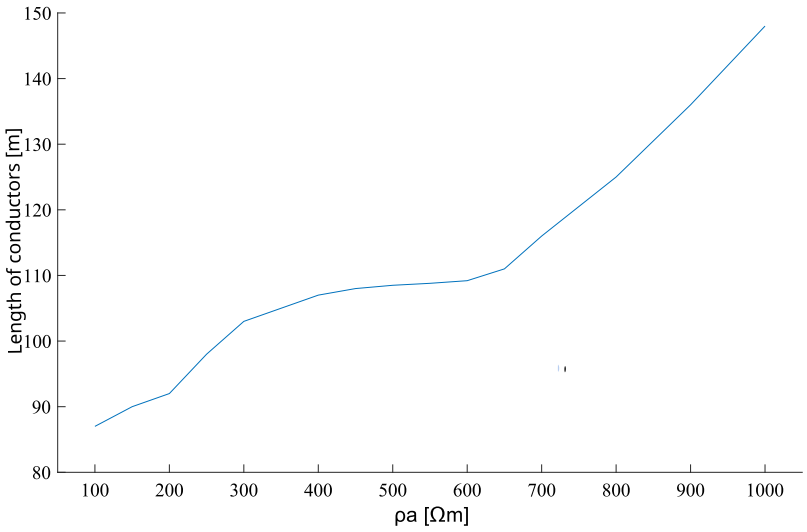


**Fig. 25.** Grid length × soil resistivity for Case study 1.

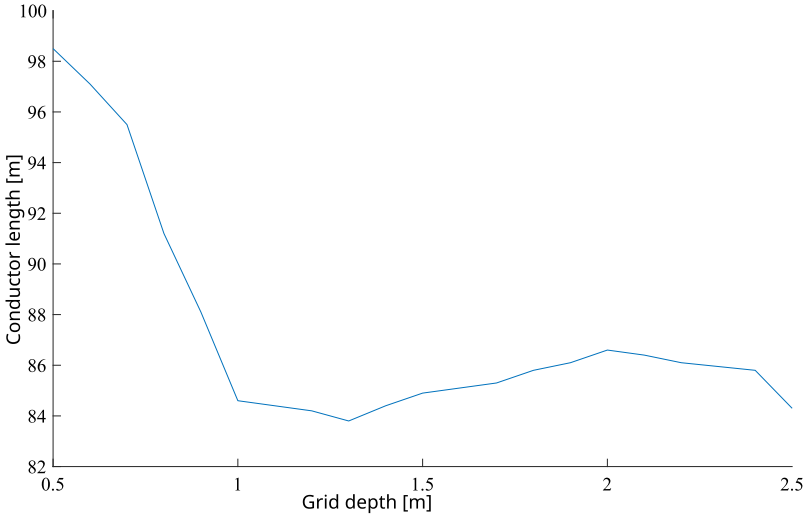


**Fig. 26.** Grid length × grid depth for Case study 2.

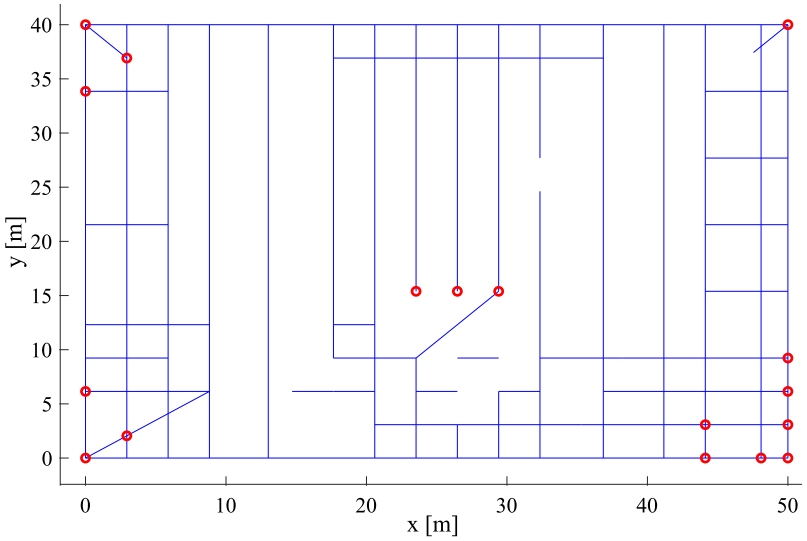


**Fig. 27.** Optimized geometry grounding grid for Case study 3, blue lines horizontal conductors and red dots vertical rods.

**Table 8**
Grounding grid parameters for Case study 3.

| | Grounding resistance [Ω] | Touch voltage [V] | Step voltage [V] | Grid length [m] | Vertical rods |
|---|---|---|---|---|---|
| GSSG-IEEE [2] | 3.718 | 665.910 | 276.170 | 910 | 43 |
| Proposed method | 2.121 | 769.453 | 221.395 | 888.789 | 17 |

**Table 9**
Parameters of the grounding grid in Case study 4.

| | Grounding resistance [Ω] | Touch voltage [V] | Step voltage [V] | Grid length [m] | Vertical rods |
|---|---|---|---|---|---|
| GSSG-IEEE [2] | 0.538 | 661.13 | 427.21 | 1100 | 27 |
| Proposed method | 0.526 | 660.21 | 103.5 | 325 | 9 |

grid, with a maximum value of 5694.851 V and a maximum GPR of 5631.715 V. Figs. 28(c) and 28(d) present the three-dimensional profile of the touch voltage and its contour within the perimeter of the grid, where the maximum touch voltage occurs at the coordinates $x = 50$ m, $y = 0$ m. Figs. 28(e) and 28(f) show the three-dimensional profile and contour of the step voltage within the perimeter of the grid, with the maximum step voltage observed at the coordinates $x_1 = 0$ m, $y_1 = 0$ m and $x_2 = 0.70711$ m, $y_2 = 0.70711$ m.

The graphical representations in Fig. 28 allow for a clear visualization of critical regions in the grounding grid area. In all subplots, the color gradients reflect voltage magnitudes, with warmer tones (yellow to orange) indicating zones of higher electrical potential. The surface voltage plots highlight localized peaks, while the touch and step voltage maps reveal the spatial distribution of hazardous areas relative to safety thresholds. These visual cues support the numerical results presented earlier and reinforce the effectiveness of the optimized configuration in managing voltage levels throughout the grid.

The calculation of the grounding mesh parameters using the proposed method resulted in $f(x)_{min} = 56.10$, while the method described in the GSSG-IEEE standard [2] yielded $f(x)_{min} = 56.71$. Furthermore, the proposed optimization method achieved a significant reduction in the number of vertical rods, approximately 60%, compared to the method described in the GSSG-IEEE standard [2]. This reduction indicates that the optimization algorithm effectively minimizes the use of vertical conductors without compromising the functionality of the grounding system.

Despite the reduction in vertical rods, the optimization method resulted in a slightly higher touch voltage 769.453 V compared to 665.910 V. This increase can be attributed to the lower energy dissipation in the soil as a result of the reduction in the number of rods. However, both the touch and the step voltages remained within the regulatory limits, demonstrating the effectiveness of the algorithm in maintaining system safety. This approach may reduce installation costs but requires careful evaluation of the balance between the number of rods and safety parameters, especially in projects aimed at minimizing costs without compromising regulatory compliance.

### 4.6. Case study 4: optimization of the grounding grid for high resistivity areas

For this case study, an area with a perimeter of 50 m × 50 m, a horizontal conductor with a cross section of 50 mm$^2$ and a grounding grid depth of 0.8 m was considered. The resistivity of the upper layer of the soil was 27 Ωm, and that of the second layer was 80 Ωm, with a thickness of 6 m for the upper layer. The current in the grid was 6000 A, the resistivity of the gravel was 3000 Ωm, and the thickness of the gravel layer was 0.1 m. The protection operation time was 0.5 s, and an angle of $\psi = 10°$ was used to calculate the step voltage. Table 9 presents the values obtained by the GSSG-IEEE method [2] and the proposed optimization method. The step and touch voltages obtained are within the regulatory limits, with 2273.829 V for the step voltage and 691.494 V for the touch voltage.

Fig. 29 shows the grid generated by the optimization algorithm, with red circles indicating the locations of the vertical rods. Figs. 30(a) and 30(b) show the surface potential within the perimeter of the grounding grid, with a maximum value of 3032.548 V and a maximum GPR of 3157.506 V. Figs. 30(c) and 30(d) present the three-dimensional touch voltage profile and its contour within the perimeter of the grid, the maximum touch voltage occurring at coordinates $x = 6.12$ m and $y = 6.12$ m. Figs. 30(e) and 30(f) show the three-dimensional step voltage profile and its contour within the perimeter of the grid, with the maximum step voltage occurring at coordinates $x_1 = 38.77$ m, $y_1 = 8.16$ m, and $x_2 = 37.77$ m, $y_2 = 8.16$ m.

The voltage distribution maps in Fig. 30 offer a visual overview of how the optimized configuration mitigates electrical hazards throughout the area of the grid. The surface potential exhibits relatively uniform behavior, while the touch and step voltage plots show well-contained peaks, particularly near the grid corners and edges. Color gradients and contour lines help to identify safe and critical zones with clarity, reinforcing the effectiveness of the proposed design in maintaining acceptable voltage levels within the operational perimeter. These visual results complement the quantitative findings and demonstrate the method's capacity to adapt to irregular conditions while ensuring safety compliance.

For the calculation of the grounding grid parameters, the method proposed by the GSSG-IEEE standard [2] resulted in $f(x)_{min} = 58.72$, while the proposed optimization method achieved $f(x)_{min} = 25.15$. The application of the optimization method led to a significant reduction in the number of horizontal conductors by 70% and a reduction 66% in the number of vertical rods, compared to the method described in the GSSG-IEEE standard [2]. This optimization not only simplifies the grid structure but also potentially reduces installation costs.

The analysis of the data in Table 9 indicates that the optimization method also significantly reduced the step voltage from 427.21 V to 103.5 V. This reduction in step voltage, along with the decrease in conductors and rods, demonstrates that the proposed optimization algorithm not only maintains safety within regulatory limits, but also improves the surface potential distribution. Although the efficiency of the optimization method is particularly evident in areas of high resistivity, it is important to ensure that these reductions do not compromise long-term safety, especially under extreme operating conditions.

### 4.7. Case study 5: grid optimization for a non-conventional perimeter area

In this case study, the area analyzed corresponds to the site where a substation was planned. Based on the proposed methodology, the project for the implementation of the grounding grid was developed. The site is located at 15°49′39.1″N, 48°03′06.6″W, where the Taguatinga Substation, owned by Neoenergia, one of the largest electricity distributors in Brazil, is currently located. Neoenergia is part of the Spanish group Iberdrola, which operates in several countries. Both projects, one following the GSSG-IEEE standard and the other utilizing the proposed methodology, were developed and submitted to the management of the substation. However, no information has been provided on the project that was implemented at the Taguatinga Substation. Fig. 31 shows the current side and top views of the site.

The area with a non-conventional perimeter is shown in Fig. 32. The horizontal conductor has a cross-sectional area of 70 mm$^2$, and the depth of the grid is 0.6 m. The resistivity of the first layer of soil is 240 Ωm, with a thickness of 9.7 m, while the second layer has a resistivity of 521.9 Ωm. The current in the grid is 2083.14 A, the resistivity of the gravel layer is 3000 Ωm, and the thickness of the gravel layer is 0.1 m. The protection operation time was 0.5 s, and the angle used for the step voltage calculation was $\psi = 10°$. Table 10 presents

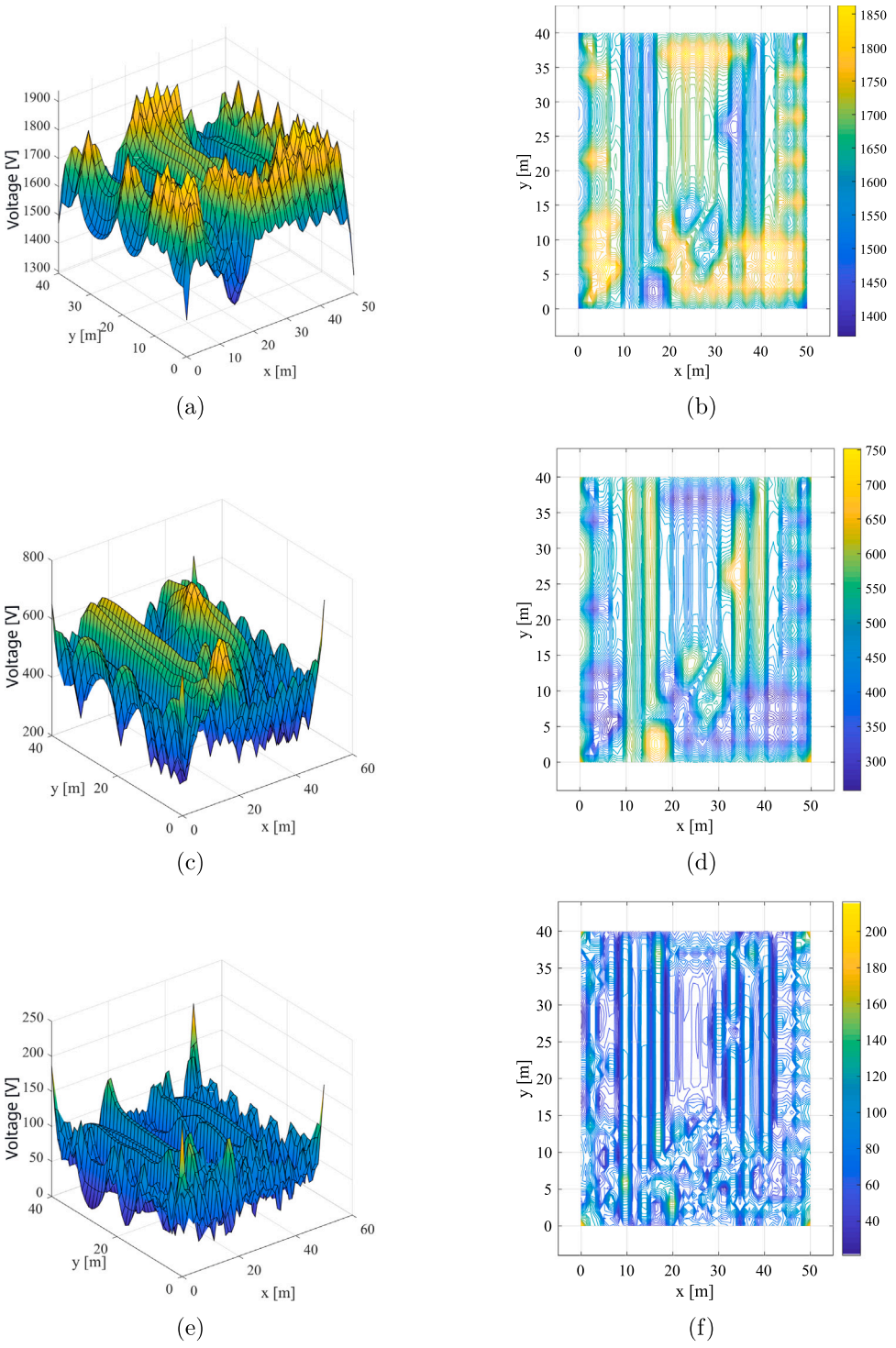


**Fig. 28.** Identification of voltages for Case study 3: (a) and (b) surface voltage, (c) and (d) touch voltage, and (e) and (f) step voltage.

the values obtained using the GSSG-IEEE standard [2] and the proposed optimization method. The step and touch voltages obtained are within the limits defined by the standards, with the step voltage at 2273.829 V and the touch voltage at 691.494 V.

Fig. 33 shows the grid generated by the optimization algorithm, with red circles indicating the locations where vertical rods will be inserted. Figs. 34(a) and 34(b) represent the surface potential within the perimeter of the grounding grid, with a maximum value of 5694.851 V and a maximum GPR of 5631.715 V. Fig. 34(c) and Fig. 34(d) present

**Table 10**
Parameters of the grounding grid in Case study 5.

| | Grounding resistance [Ω] | Touch voltage [V] | Step voltage [V] | Grid length [m] | Vertical rods |
|---|---|---|---|---|---|
| GSSG-IEEE [2] | 2.38 | 652.41 | 219.60 | 2100 | 0 |
| Proposed method | 2.73 | 638.54 | 221.05 | 1253 | 8 |

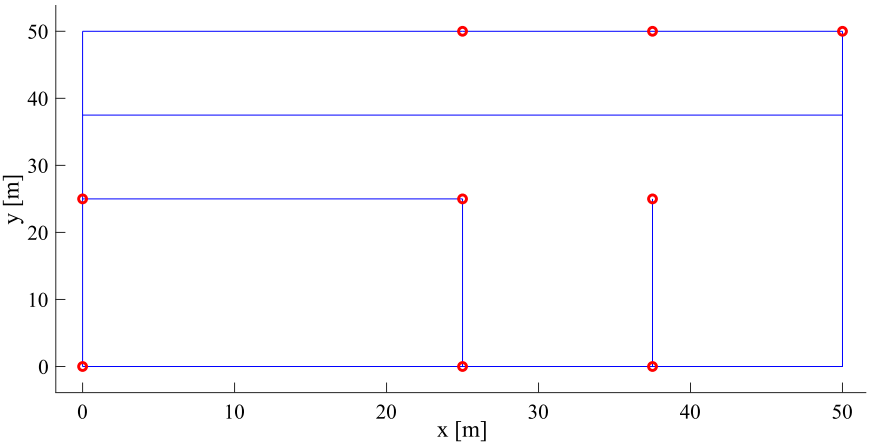


**Fig. 29.** Optimized geometry grounding grid for Case study 4, blue lines horizontal conductors and red dots vertical rods.

the three-dimensional touch voltage profile and its contour within the perimeter of the grid, with the maximum touch voltage found at coordinates $x = 1.01$ m and $y = 44.47$ m. Figs. 34(e) and 34(f) illustrate the three-dimensional step voltage profile and its contour within the perimeter of the grid, with the maximum step voltage located at coordinates $x_1 = 76.81$ m, $y_1 = 5.05$ m and $x_2 = 77.52$ m, $y_2 = 5.76$ m. The calculation of the grounding grid parameters using the method proposed by the GSSG-IEEE standard [2] resulted in $f(x)_{min} = 33.19$, while the proposed optimization method achieved $f(x)_{min} = 32.69$.

The voltage maps in Fig. 34 illustrate how the proposed method handles complex grid geometries with irregular boundaries. Despite the asymmetry of the perimeter, the distribution of surface, touch, and step voltages remains spatially coherent, with the highest values concentrated near specific regions but still within a well-defined contour pattern. The use of color gradients and contour lines effectively highlights critical zones, helping to identify areas that require reinforcement. These visualizations demonstrate the robustness of the optimization approach, especially in scenarios where conventional square section constraints are no longer applicable.

The proposed optimization method resulted in a 40% reduction in the number of horizontal conductors compared to the GSSG-IEEE standard method [2]. This significant decrease demonstrates the algorithm's ability to optimize the grounding grid, making it more material efficient. The simulation time for this optimization was sixteen hours and fifteen minutes, reflecting the process's complexity and the need for extended processing to achieve better solutions, ideally with a higher maximum number of generations. Another relevant factor is the division of the grid into square sections when using the GSSG-IEEE standard [2], as the electrodes must only form right angles.

In addition to the reduction in conductors, the analysis of the data in Table 10 indicates that the optimization method resulted in a slightly higher grounding resistance of 2.73 Ω compared to 2.38 Ω using the GSSG-IEEE standard method [2]. However, this difference is offset by the significant reduction in the grid length, from 2100 m to 1253 m, and the introduction of only eight vertical rods. This suggests that the optimization method does not compromise safety, as it maintains touch and step voltages within regulatory limits while offering a more economical and simplified solution, particularly suitable for situations where cost reduction is a priority.

To assess the efficiency of the optimization process, Fig. 35 presents the convergence curve of the evaluation function over the generations of the algorithm for the three case studies analyzed. The horizontal axis represents the number of generations, while the vertical axis displays the values of the objective function, $f(x)$, at each iteration. In all cases, a progressive reduction in the evaluation function is observed over generations, indicating continuous improvement in the solutions found by the algorithm. In Case Study 3, convergence occurs rapidly during the initial generations, stabilizing after approximately 20 iterations. In Case Study 4, the evaluation function shows a more pronounced decrease in the early generations but continues with minor variations until reaching a stable value around generation 27. Case Study 5 follows a similar pattern, with a significant drop in initial cycles, followed by a gradual stabilization.

The variation in convergence rates among the case studies is attributed to differences in the characteristics of the grounding grid and the soil conditions in each configuration. The behavior of the curves confirms the effectiveness of the algorithm in identifying optimized solutions, ensuring that the grid meets the established safety and performance criteria.

Regarding the experimental conditions, the study was conducted to validate the optimization of the grounding grid. The experimental setup consisted of a test site with irregular geometric characteristics, where the grounding grid was designed and analyzed. Data collection was carried out using a digital earth resistance tester, model Megabras EM4058, capable of measuring the ground resistance $R_{ground}$ and the apparent electrical resistivity of the soil $\rho_a$ at different current frequencies, specifically 270 Hz, 570 Hz, 870 Hz, 1170 Hz and 1470 Hz. This device conducts a measurement sweep and displays the average value on its screen, ensuring accuracy in the analyzes. The measurement range ranges from 0.01 Ω to 20 kΩ, with an accuracy of ±2% for $R_m \leq 2$ kΩ and ±5% for $R_m > 2$ kΩ. The soil properties were previously characterized through electrical resistivity measurements using the Wenner array at multiple points, allowing terrain stratification modeling and adaptation of the computational model for optimization simulation.

The experimental process followed a structured sequence of steps. Initially, the grounding grid was installed with conventional parameters and grounding resistance measurements, as well as touch and step voltages, were performed using the EM4058 earth resistance tester. Subsequently, variations in the grid parameters were applied according to the optimization algorithm, followed by new measurements to assess the impact of these modifications. The tested configurations were compared in terms of performance, with a focus on reducing grid impedance and ensuring compliance with regulatory requirements. The results demonstrated that the optimized approach led to a significant reduction in impedance compared to the initial configuration, ensuring improved efficiency and safety.

### 4.8. Discussion

The results confirm the efficiency of the proposed methodology in optimizing grounding grids for different configurations, enabling reductions of up to 66% in the number of vertical rods for Case Study 3 and Case Study 4 and 40% in the number of horizontal conductors for Case Study 5, compared to conventional methods described in the

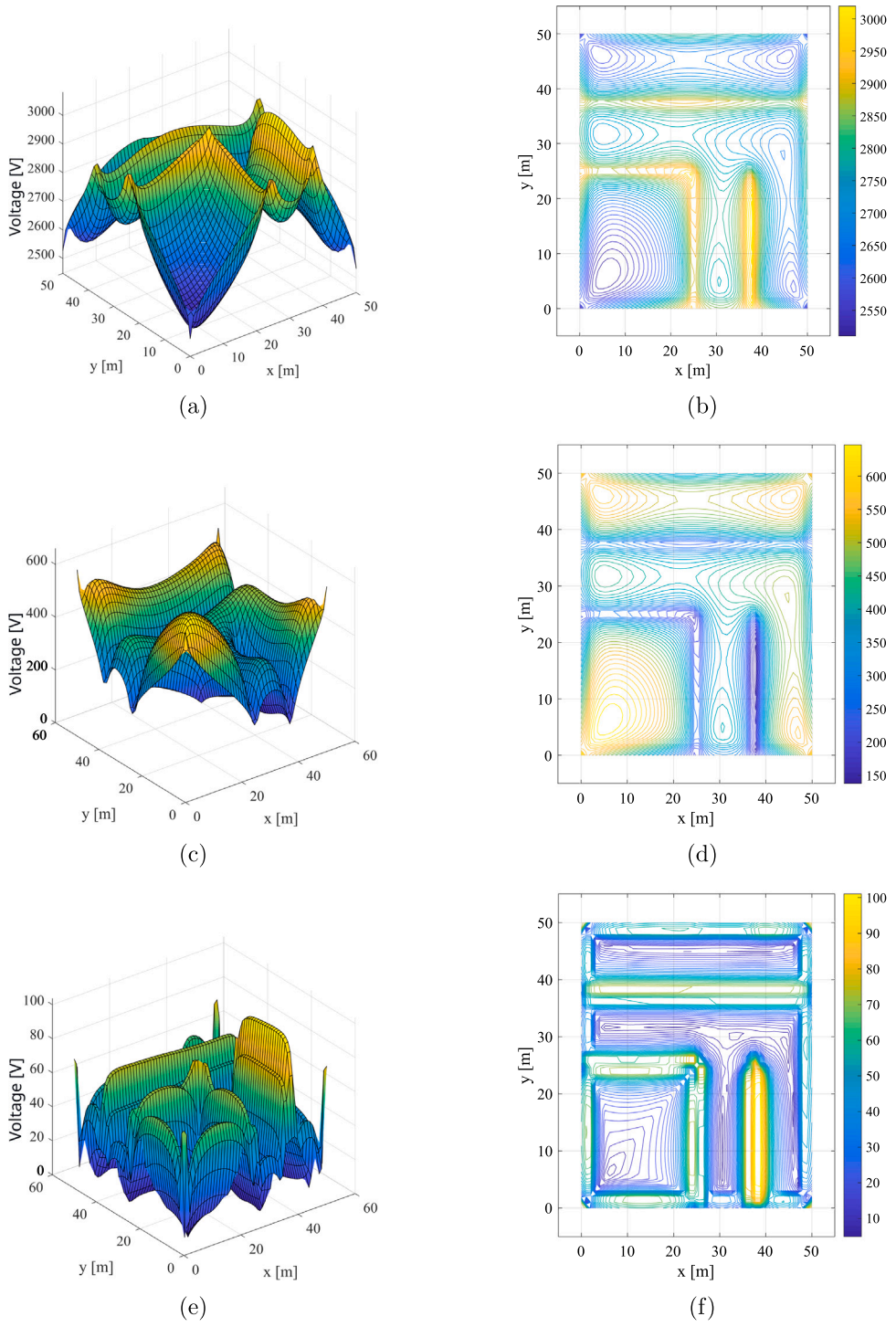


**Fig. 30.** Identification of voltages in Case study 4: (a) and (b) surface voltage, (c) and (d) touch voltage, and (e) and (f) step voltage.

GSSG-IEEE [2]. These reductions lead to cost savings, ensure that touch and step voltages remain within regulatory limits, enhance system stability, and reduce the risk of grounding failures while maintaining compliance with electrical safety standards. These findings suggest that the proposed algorithm can generate optimized geometries for various soil conditions and irregular perimeters, making it a promising alternative for industrial applications, including substations and automated facilities.

This result gains further relevance when compared with recent literature on applications of artificial intelligence in power systems. Studies such as Wang et al. [70] review approaches based on neural networks, support vector machines, and evolutionary algorithms, primarily focused on fault identification in distribution networks. These works concentrate on signal analysis and do not address the structural modeling or physical geometry of grounding meshes. Similarly, Na Wang [71] employed an Artificial Bee Colony algorithm combined with


**Fig. 31.** Area of Case Study 5: (a) side view and (b) top view.

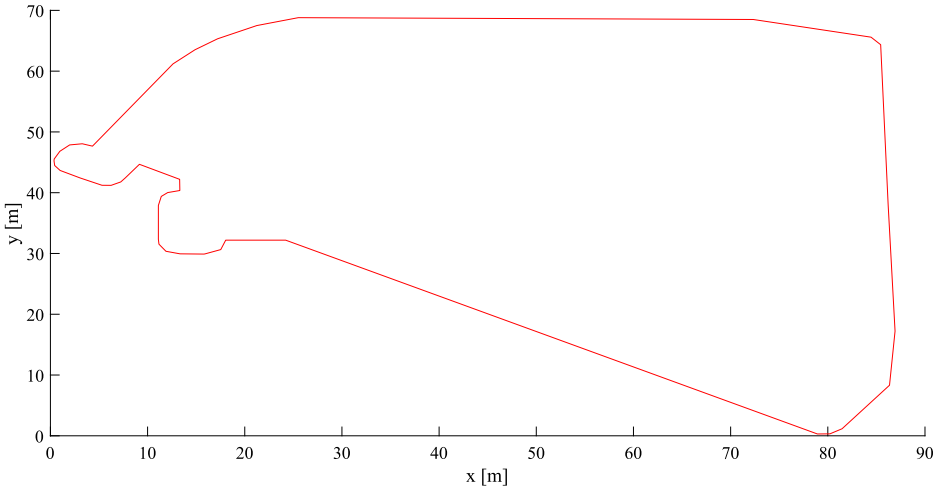


**Fig. 32.** Non-conventional area and perimeter for the grounding grid in Case study 5.

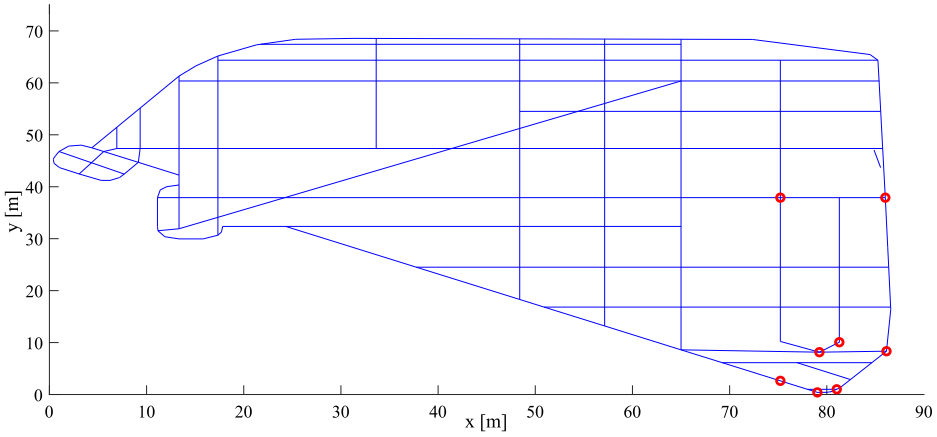


**Fig. 33.** Optimized geometry grounding grid for Case study 5, blue lines horizontal conductors and red dots vertical rods.

deep neural networks to classify faulty lines in low-current grounding systems, without proposing any structural modifications to the grounding grid.

In this context, the contribution of the present study is emphasized by employing evolutionary algorithms for the geometric design of grounding meshes, integrating both horizontal conductors and vertical rods throughout stratified soil layers. The proposed approach enables adaptation to irregular perimeters and promotes a reduction in the number of conductive materials while ensuring compliance with technical and regulatory standards. Whereas studies such as those by Venkatachalam [72] and Anwar et al. [73] focus on fault classification using supervised models, the present work addresses an earlier stage: the optimized geometric design of the grounding grid, an aspect still underexplored in the specialized literature.

The analysis of the influence of soil resistivity on grid length in Case Study 1 demonstrated that optimization is highly dependent on the characteristics of the soil. For resistivity values below 100 Ωm, there is an almost linear relationship between the length of the network and the resistance to grounding. However, for higher resistivity values, the efficiency of adding horizontal conductors decreases, making the use

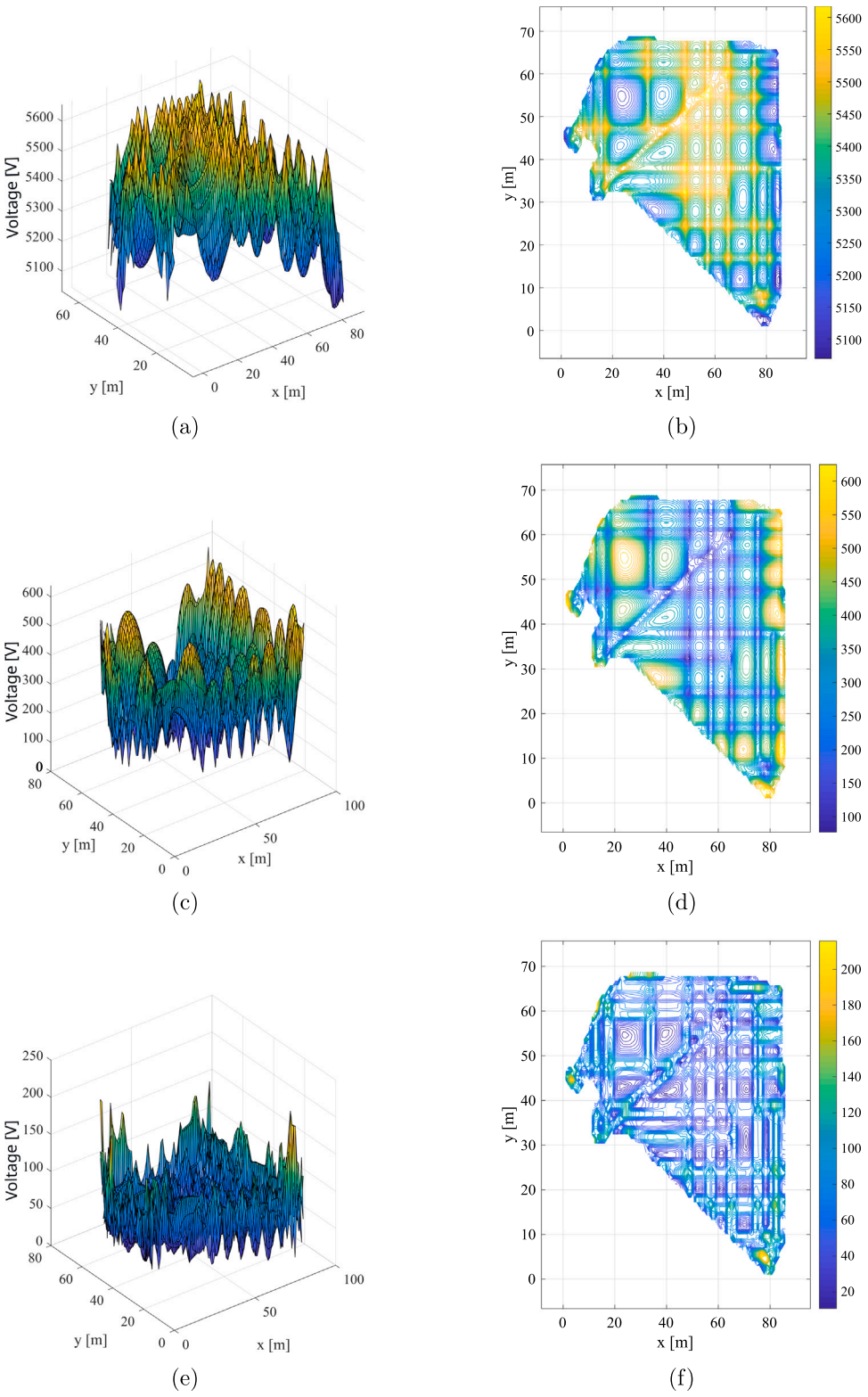


**Fig. 34.** Identification of voltages in Case study 5: (a) and (b) surface voltage, (c) and (d) touch voltage, and (e) and (f) step voltage.

of vertical rods necessary to maintain acceptable resistance levels [74]. This behavior highlights the importance of accurately modeling soil properties to optimize conductor distribution.

In Case Study 2, which examined the influence of grid depth, it was observed that increasing conductor depth reduces grounding resistance, particularly in high-resistivity soils [75,76]. However, this effect is less significant in low-resistivity soils, where additional depth has limited impact. This analysis provides design guidelines by identifying conditions under which increasing depth is advantageous and when the use of vertical rods is more effective.

Case Study 3, Case Study 4, and Case Study 5 focused on optimizing grounding grids in challenging scenarios, including extensive perimeters, high-resistivity soils, and non-conventional geometries. The proposed approach resulted in an average reduction of 35% in the total

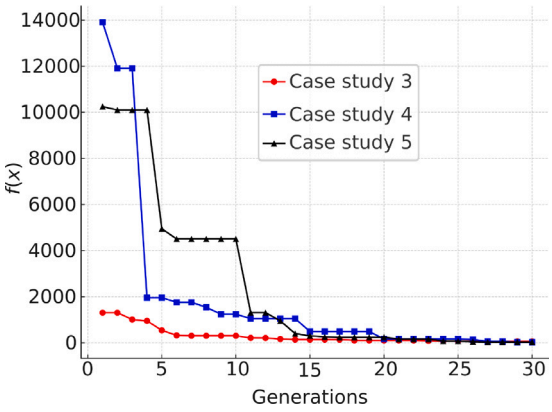


**Fig. 35.** Convergence curves of the optimization algorithm for the three case studies.

number of conductors while ensuring that the touch and step voltages remained within the regulatory limits. A comparison with conventional methods demonstrated that redistributing conductors in an adaptive configuration enhances electrical efficiency and reduces installation costs.

A comparative analysis with well-established methods in the literature confirms the efficiency of the proposed optimization approach. Classical techniques, such as the Heppe method [39], employ the complex image method to calculate surface potentials, producing accurate results for homogeneous and stratified soils. However, these methods are generally limited to predefined geometries with uniform conductor spacing. The proposed methodology advances this field by optimizing conductor placement and angular distribution and improving adaptability to nonconventional grid layouts. Although in certain cases, such as Case Study 5, the grounding resistance obtained is slightly higher than that of conventional approaches, this trade-off is justified by substantial reductions in material usage and installation costs. Moreover, the algorithm allows regulator voltage thresholds to be adjusted, ensuring compliance with different operational constraints.

The validation of the simulator using experimental data from the literature confirmed the consistency of the methodology in modeling grounding impedance and potential distribution. The results exhibited a mean error below 5% compared to the reference data, ensuring the reliability of the numerical model [77]. This outcome underscores the accuracy of the approach and validates its applicability in the analysis and design of electrical grounding systems. Compared to traditional methods, the proposed model offers greater flexibility by incorporating varied geometries and different soil conditions, making it more suitable for complex scenarios.

The study demonstrated that integrating horizontal conductors with strategically placed vertical rods enhances grounding performance in high-resistivity soils. This optimization achieved a 28% reduction in grounding resistance compared to conventional configurations. However, in extremely high-resistivity soils, additional measures, such as soil enhancement materials, may be necessary to meet safety standards [3]. In Case Study 5, the optimized configuration reduced the total conductor length from 2100 m to 1253 m, maintaining regulatory compliance. Although ground resistance increased slightly from 2.38 Ω to 2.73 Ω, the potential distribution remained stable, preventing localized high-voltage points. These findings confirm the adaptability of the proposed methodology to industrial applications with geometric constraints.

The proposed methodology enhances the adaptability to various soil conditions while maintaining computational efficiency and compliance with safety standards. Unlike conventional methods, which focus on uniform conductor spacing to achieve homogeneous surface potential distribution [38], the proposed approach prioritizes material efficiency. This optimization may introduce minor variations in potential uniformity, as observed in Case Study 3. However, these variations remain within acceptable limits and can be adjusted when stricter uniformity is required. This balance between efficiency and electrical safety makes the method particularly suitable for industrial environments with geometric constraints.

The primary contribution of this study lies in the optimization of grounding grids for non-conventional areas and stratified soils with multiple layers, a topic that has received limited attention in the existing literature. The development of an adaptive optimization algorithm enables solutions that not only comply with regulatory requirements but also provide practical advantages for complex industrial environments. The flexibility and cost-effectiveness of the proposed approach make it particularly suitable for applications in substations and industrial facilities, where efficiency and safety are paramount.

While the proposed methodology offers significant advantages, it also presents some challenges. A key limitation is the sensitivity of the optimization algorithm to the weighting factors in the objective function. In high-resistivity soils, as seen in Case Study 1, convergence instability may occur, necessitating manual adjustments to ensure consistent results. Furthermore, for complex optimizations like Case Study 5, computational costs were relatively high, emphasizing the need for enhanced processing capabilities for large-scale applications. Another limitation is the omission of capacitive effects at high frequencies, such as those that occur during lightning discharges. More research is required to address this aspect and extend the applicability of the method to all operational conditions.

Several strategies can mitigate these limitations. The use of pattern recognition techniques for dynamic adjustment of objective function weights can enhance algorithm stability, minimizing the need for manual intervention. Furthermore, hybrid approaches that integrate particle swarm optimization (PSO) with neural networks could accelerate convergence and reduce simulation time. To account for capacitive effects at high frequencies, incorporating high-frequency modeling techniques would enable a more comprehensive evaluation of grounding systems under different operational conditions.

## 5. Conclusion

This work introduces an innovative approach to optimize the geometry of electrical grounding grids using variable-sized matrices to generate populations. The methodology was applied at industrial frequencies of 50 Hz and 60 Hz, allowing the optimization of horizontal conductors with varying angles and spacing, as well as the positioning of vertical rods in stratified soils. The proposed method not only reduces the construction costs of grounding grids but also minimizes implementation time, making it highly suitable for automated industrial environments where efficiency and reliability are essential. By providing optimized grounding configurations that adapt to diverse soil conditions, this methodology supports the development of resilient and fault-tolerant automation systems, ultimately improving the stability and safety of industrial operations.

The hypothesis suggesting the feasibility of optimizing grounding grids with arbitrary geometry in stratified soils was validated throughout this study. All planned stages, from literature review to computational implementation, were successfully completed, achieving the proposed objectives. The mathematical modeling was adjusted to incorporate GPR as a variable, and the developed algorithm enabled the creation of optimized grids within a predefined perimeter, demonstrating the method's efficiency.

The results confirmed the advantages of the method, such as its ability to calculate grid parameters with electrodes in arbitrary positions, handle non-uniform current distribution, and provide a detailed analysis of performance across different regions of the grid. Furthermore, the method proved to be efficient in optimizing the use of conductors and rods, resulting in cost savings and a reduction in inductive effects.

Therefore, it is concluded that the proposed method offers a robust and versatile solution for grounding grid optimization, despite the challenges of implementation and processing time, which open avenues for future improvements.

## CRediT authorship contribution statement

**Carlos Leandro Borges da Silva:** Writing – original draft, Visualization, Validation, Supervision, Software, Resources, Methodology, Investigation, Funding acquisition, Data curation, Conceptualization. **Thyago Gumeratto Pires:** Writing – original draft, Visualization, Validation, Supervision, Software, Resources, Methodology, Investigation, Formal analysis, Data curation, Conceptualization. **Antonio Marcelino Silva Filho:** Visualization, Validation, Supervision, Software, Resources, Methodology, Investigation, Formal analysis, Data curation, Conceptualization. **Junio Santos Bulhões:** Visualization, Validation, Software, Resources. **Orlando M. Oliveira Belo:** Writing – review & editing, Visualization, Validation, Software, Resources. **Clóves Gonçalves Rodrigues:** Visualization, Validation, Software, Resources. **Antonio Paulo Coimbra:** Writing – review & editing, Visualization, Validation, Software, Resources, Formal analysis. **Wesley Pacheco Calixto:** Writing – review & editing, Writing – original draft, Visualization, Validation, Supervision, Software, Resources, Project administration, Methodology, Investigation, Funding acquisition, Formal analysis, Data curation, Conceptualization.

## Declaration of competing interest

The authors declare that we have no financial interests or conflicts of interest that could potentially influence the objectivity, integrity, or impartiality of our research findings. Specifically:

1. Financial Support: The research conducted and the preparation of this manuscript received no external financial support, grants, or funding from any public or private entity.

2. Patents: We confirm that there are no patents associated with the research work presented in this manuscript, and no patent applications have been submitted during the course of this study.

3. Salary Reimbursement: The authors involved in this research project have not received any salary, fees, or reimbursements related to the publication of this work. The research was conducted as part of our academic and professional activities, and no financial compensation has been sought or received.

We hereby affirm that this Declaration of Interest accurately reflects our financial and non-financial relationships, and we acknowledge our responsibility to promptly inform the editorial board of any changes in our circumstances that may impact this declaration during the review process.

## Acknowledgments

This work is financed by national funds through FCT - Fundação para a Ciência e a Tecnologia, Portugal, I.P., under the projects UIDB/00048/2020 (DOI 10.54499/UIDB/00048/2020), National Council for Scientific and Technological Development (CNPq/Brazil) for the contribution in the form of a Productivity Scholarship in Research, process: 301644/2022-5, and Brazilian Federal Agency for Support and Evaluation of Graduate Education (CAPES/Brazil) for a doctoral scholarship, process: 88887.927817/2023-00.

## Data availability

Data will be made available on request.

## References

[1] L. Zhang, J. Yuan, Z. Li, The complex image method and its application in numerical simulation of substation grounding grids, Commun. Numer. Methods Eng. 15 (11) (1999) 835–839.

[2] IEEE, Guide for Safety in AC Substation Grounding, (Revision of IEEE Std 80-2000/Incorporates IEEE Std 80-2013), first ed., IEEE, 3 Park Avenue, New York, NY 10016-5997, USA, 2015.

[3] A.M. Silva Filho, C.G. Rodrigues, O.M.O. Belo, A.P. Coimbra, V.M.G. Pacheco, W.P. Calixto, Measurement of grounding resistance over a seasonal cycle with hygroscopic materials in the encapsulation of grounding rods, Measurement (2025) 116767.

[4] M. Unde, B. Kushare, Impact of seasonal variation of soil resistivity on safety of substation grounding system, in: Fifth International Conference on Advances in Recent Technologies in Communication and Computing, ARTCom 2013, Institution of Engineering and Technology, 2013, pp. 173–182.

[5] N. Bhardwaj, O. Rahi, M. Sharma, Seasonal influence on the substation grounding grid performance and its optimal design to neutralize the influence, in: 2016 IEEE 1st International Conference on Power Electronics, Intelligent Control and Energy Systems, ICPEICES, IEEE, 2016, pp. 1–5.

[6] P. Navinesshani, O. M., M.A. A., K. M., The impact of substation grounding grid design parameters in non-homogenous soil to the grid safety threshold Parameters, IEEE Access (2021).

[7] N. Permal, M. Osman, A.M. Ariffin, M.Z. Abidin Ab Kadir, Effect of non-homogeneous soil characteristics on substation grounding-grid performances: A review, Appl. Sci. 11 (16) (2021) 7468.

[8] G. Gilbert, Y.L. Chow, D.E. Bouchard, M.M.A. Salama, Optimization of high voltage substations using a random walk technique, in: 2011 IEEE PES 12th International Conference on Transmission and Distribution Construction, Operation and Live-Line Maintenance, ESMO, IEEE, 2011, pp. 1–7.

[9] Hyung-Soo Lee, Jung-Hoon Kim, F. Dawalibi, Jinxi Ma, Efficient ground grid designs in layered soils, IEEE Trans. Power Deliv. 13 (3) (1998) 745–751.

[10] P.R. Bonda, M.K. Mishra, Optimized design of earthing system for substations with high soil resistivity and limited plot area, in: 2018 20th National Power Systems Conference, NPSC, IEEE, 2018, pp. 1–6.

[11] I. Colominas, J.M. Blanco, F. Navarrina, M. Casteleiro, A BEM formulation for computational design of grounding systems instratified soils, 1998.

[12] F. Navarrina, I. Colominas, M. Casteleiro, Why do computer methods for grounding analysis produce anomalous results? in: IEEE Power Engineering Society General Meeting, 2004, vol. 2, IEEE, 2003, 1044–1044.

[13] L. Neamt, O. Matei, O. Chiver, Finite element method combined with neural networks for power system grounding investigation, Int. J. Adv. Comput. Sci. Appl. 8 (2) (2017).

[14] L.G. Rodrigues, I.M. dos Santos, M. Tello, D.S. Gazzana, Grounding grid resistance estimation in non- homogeneous oils: A Study Focused on Equivalent Analytical Models, in: 2021 IEEE International Conference on Environment and Electrical Engineering and 2021 IEEE Industrial and Commercial Power Systems Europe, EEEIC/I&CPS Europe, IEEE, 2021, pp. 1–5.

[15] G. Aiello, S. Alfonzetti, S.A. Rizzo, N. Salerno, Efficient analysis of grounding systems by means of the hybrid FEM–DBCI method, IEEE Trans. Ind. Appl. 51 (6) (2015) 5159–5166.

[16] J.P.C.F. Ivo, C.M. Moraes, A.G. Martins-Britto, Enhanced circuit-theory-based model for accurate simulation of electrically large grounding systems, in: 2023 Workshop on Communication Networks and Power Systems, WCNPS, IEEE, 2023, pp. 1–7.

[17] A. Habjanic, M. Trlep, Optimal design of the grounding grid by FEM considering different layered soil models, Prz. Elektrotech. 8 (7) (2007) 112–114.

[18] M. Mishra, B. Patnaik, M. Biswal, S. Hasan, R.C. Bansal, A systematic review on DC-microgrid protection and grounding techniques: Issues, challenges and future perspective, Appl. Energy 313 (2022) 118810.

[19] U.U. Uma, L.O. Uzoechi, B.J. Robert, Optimization design of ground grid mesh of 132/33 kV sustation using ETAP, Niger. J. Technol. 35 (4) (2016) 926–934.

[20] S.S. Ghoneim, I.B. Taha, Control the cost, touch and step voltages of the grounding grids design, IET Sci. Meas. & Technol. 10 (8) (2016) 943–951.

[21] O. Gouda, G. Amer, O. Salim, E. Elsayed, Techniques used for unequally spaced grounding grid design, J. Multidiscip. Res. Rev. 1 (1) (2018) 1–9.

[22] V.K. Voon, K.I. Wong, T.C. Tiong, A. Mansour, K.H. Law, Grounding grid design in electrical power substation using optimization methods, IOP Conf. Ser.: Mater. Sci. Eng. 495 (2019) 012037.

[23] S. Kara, O. Kalenderli, O. Altay, Optimum grounding grid design by using genetic algorithms, in: 2015 9th International Conference on Electrical and Electronics Engineering, ELECO, IEEE, 2015, pp. 1117–1121.

[24] S. Ghoneim, H. Hirsch, A. Elmorshedy, R. Amer, Optimum grounding grid design by using an evolutionary algorithm, in: 2007 IEEE Power Engineering Society General Meeting, IEEE, 2007, pp. 1–7.

[25] W.P. Calixto, L.M. Neto, M. Wu, K. Yamanaka, E. da Paz Moreira, Parameters estimation of a horizontal multilayer soil using genetic algorithm, IEEE Trans. Power Deliv. 25 (3) (2010) 1250–1257.

[26] A.F. Otero, J. Cidrás, C. Garrido, Grounding grid design using evolutionary computation-based methods, Electr. Power Components Syst. 30 (2) (2002) 151–165.

[27] C.L.B. Silva, D.N. Oliveira, T.G. Pires, J.W.L. Nerys, P.H.S. Barbosa, W.P. Calixto, A.J. Alves, Optimization of grounding grid's multidesign geometry, in: 2016 IEEE 16th International Conference on Environment and Electrical Engineering, EEEIC, IEEE, 2016, pp. 1–6.

[28] Z. He, X. Wen, J. Wang, Optimization design of substation grounding grid based on genetic algorithm, in: Third International Conference on Natural Computation, ICNC 2007, IEEE, 2007, pp. 140–144.

[29] W.P. Calixto, A.P. Coimbra, B. Alvarenga, J.P. Molin, A. Cardoso, L.M. Neto, 3-D soil stratification methodology for geoelectrical prospection, IEEE Trans. Power Deliv. 27 (3) (2012) 1636–1643.

[30] E.M. Elrefaie, S. Ghoneim, M. Kamal, R. Ghaly, Evolutionary strategy technique to optimize the grounding grids design, in: 2012 IEEE Power and Energy Society General Meeting, IEEE, 2012, pp. 1–6.

[31] H. Khodr, G. Salloum, V. Miranda, Grounding system design in electrical substation: An optimization approach, in: 2006 IEEE/PES Transmission & Distribution Conference and Exposition: Latin America, IEEE, 2006, pp. 1–5.

[32] X. Wu, Q. Zhang, Jiahong He, Substation grounding system optimization with utilizing a novel MATLAB application, in: 2016 IEEE PES Asia-Pacific Power and Energy Engineering Conference, APPEEC, IEEE, 2016, pp. 628–633.

[33] F. Aboura, O. Touhami, Grounding system cost reduction using multi-objective optimisation method, IET Sci. Meas. & Technol. 14 (10) (2020) 893–900.

[34] C. Cardoso, N. Filipe, Andréia, An integrated methodology for design of grounding systems, 2015.

[35] M. Tello, D.S. Gazzana, V.B. Tello, L.T.C. Pulz, R.C. Leborgne, A.S. Bretas, Substation grounding grid diagnosis applying optimization techniques based on measurements and field tests, IEEE Trans. Ind. Appl. 56 (2) (2020) 1190–1196.

[36] H.B. Dwight, Calculation of resistances to ground, Trans. Am. Inst. Electr. Eng. 55 (12) (1936) 1319–1328.

[37] G.W. Howe, Capacity of radio-telegraph antenna, Electr. 73 (1) (1914) 829–859.

[38] J.G. Sverak, Optimized grounding grid design using variable spacing technique, Trans. Power Appar. Syst. PAS-95 (1) (1976) 362–374.

[39] A. Heppe, Computation of potential at surface above an energized grid or other electrode, allowing for non-uniform current distribution, Trans. Power Appar. Syst. PAS-98 (6) (1979) 1978–1989.

[40] P. Kouteynikoff, Numerical computations of the grounding resistance of substations and towers, Trans. Power Appar. Syst. 3 (3) (1980) 957–965.

[41] D.L. Garrett, J.G. Pruitt, Problems encountered with the average potential method of analyzing substation grounding systems, Trans. Power Appar. Syst. PAS-104 (12) (1985) 3585–3596.

[42] T. Takahashi, T. Kawase, Calculation of earth resistance for a deep-driven rod in a multi-layer earth structure, Trans. Power Deliv. 6 (2) (1991) 608–614.

[43] F. Dawalibi, N. Barbeito, Measurements and computations of the performance of grounding systems buried in multilayer soils, Trans. Power Deliv. 6 (4) (1991) 1483–1490.

[44] Y. Chow, M.M.A. Salama, A simplified method for calculating the substation grounding grid resistance, Trans. Power Deliv. 9 (2) (1994) 736–742.

[45] M.M. Elsherbiny, Y.L. Chow, M.M.A. Salama, A fast and accurate analysis of grounding resistance of a driven rodbed in a two-layer soil, Trans. Power Deliv. 11 (2) (1996) 808–814.

[46] T.G. Pires, C.L. Silva, D.N. Oliveira, J.W. Nerys, A.J. Alves, W.P. Calixto, Computation of grounding grids parameter on unconventional geometry, in: 2015 CHILEAN Conference on Electrical, Electronics Engineering, Information and Communication Technologies, CHILECON, IEEE, 2015, pp. 523–527.

[47] R.S. Nikjoo, S.H.H. Sadeghi, R. Moini, A hybrid genetic-simulated annealing algorithm for optimal design of grounding grids with rods, in: 2010 Asia-Pacific Power and Energy Engineering Conference, IEEE, 2010, pp. 1–4.

[48] S. Freddy, M. Sinchi, P. Flavio, A. Quizhpi, C. Hernan, P. Guillen, N. Sandra, N. Quinde, Soil treatment to reduce grounding resistance by applying low-resistivity material (LRM) and chemical ground electrode in different grounding systems configurations, in: 2018 IEEE International Autumn Meeting on Power, Electronics and Computing, ROPEC, IEEE, 2018, pp. 1–6.

[49] B. Thapar, V. Gerez, A. Balakrishnan, D. Blank, Simplified equations for mesh and step voltages in an AC substation, Trans. Power Deliv. 6 (2) (1991) 601–607.

[50] A. Covitti, G. Delvecchio, A. Fusco, F. Lerario, F. Neri, Two cascade genetic algorithms to optimize unequally spaced grounding grids with rods, Int. Conf. Comput. Tool 2 (1) (2005) 1533–1536.

[51] Y.-m. Yang, M.-f. Peng, H.-t. Hong, Y.-h. Yuan, Optimal design of grounding grids based on genetic algorithm, in: 2009 Third International Conference on Genetic and Evolutionary Computing, IEEE, 2009, pp. 129–132.

[52] M. Caldora Costa, M. Leite Pereira, Y. Marechal, J. Coulomb, J. Cardoso, Optimization of grounding grids by response surfaces and genetic algorithms, IEEE Trans. Magn. 39 (3) (2003) 1301–1304.

[53] M. Ya'acob, L. Lu, S. Zulkifli, N. Roslan, W.W. Ahmad, Agrivoltaic approach in improving soil resistivity in large scale solar farms for energy sustainability, Appl. Energy 352 (2023) 121943.

[54] A.F. Andrade, E.G. da Costa, M.F. Gonçalves, G.R. Lira, R.O. Teixeira, Modeling grounding systems response to current impulses considering nonlinear effects, IEEE Trans. Power Deliv. 36 (6) (2021) 3858–3866.

[55] E.D. Sunde, Earth Conduction Effects in Transmission Systems, first ed., vol. 1, Dover Publications, New York, 1968.

[56] W.K. Switzer, Practical guide to electrical grounding, 1999, An ERICO Publication First Printing.

[57] M.A. Salam, Q.M. Rahman, et al., Power Systems Grounding, Springer, 2016.

[58] R. Roeper, Short-circuit currents in three-phase networks, 1972, Kurzschlußströme in Drehstromnetzen, Engl.-Transl. from the 5. Rev. German Ed. by Translation Office of Siemens AG., Erlangen.

[59] A.A. Zaky, An Introduction to Safety Grounding, CRC Press, 2021.

[60] G. Vijayaraghavan, M. Brown, M. Barnes, Practical Grounding, Bonding, Shielding and Surge Protection, Elsevier, 2004.

[61] R. Morrison, Grounding and Shielding: Circuits and Interference, John Wiley & Sons, 2016.

[62] P. Sarajcev, S. Vujevic, A review of methods for grounding grid analysis, in: SoftCOM 2009-17th International Conference on Software, Telecommunications & Computer Networks, IEEE, 2009, pp. 42–49.

[63] F. Wenner, A Method of Measuring Earth Resistivity, vol. 258, US Department of Commerce, Bureau of Standards, 1916.

[64] C.F. Dalziel, Efect of electric shock on man, Electr. Eng. 60 (1941) 63–66.

[65] G. Campbell, Mutual Inductances of Circuits Composed of Straight Wires, Physical Review, 1915.

[66] N. Patankar, H.G. Fell, A.R. de Queiroz, J. Curtis, J.F. DeCarolis, Improving the representation of energy efficiency in an energy system optimization model, Appl. Energy 306 (2022) 118083.

[67] G. Lu, W. Fan, D. Lu, T. Zhao, Q. Wu, M. Liu, Z. Liu, Lung-inspired hybrid flow field to enhance PEMFC performance: A case of dual optimization by response surface and artificial intelligence, Appl. Energy 355 (2024) 122255.

[68] S.S.M. Ghoneim, Optimization of Grounding Grids Design with Evolutionary Strategies first ed., (Ph.D. thesis), Faculty of Enginnering Sciences, Univeristät Duisburg-Essen, Duisburg, Germany, 2007.

[69] J. Endrenyi, Evaluation or resistivity tests for design of station grounds in nonunirorm soil, IEEE Trans. Power Appar. Syst. (1963).

[70] F. Wang, Z. Zhang, K. Wu, D. Jian, Q. Chen, C. Zhang, Y. Dong, X. He, L. Dong, Artificial intelligence techniques for ground fault line selection in power systems: State-of-the-art and research challenges, Math. Biosci. Eng. 20 (8) (2023) 14518–14549.

[71] N. Wang, Fault line selection of power distribution system via improved bee colony algorithm based deep neural network, Energy Rep. 8 (2022) 43–53.

[72] Y. Venkatachalam, T. Subbaiyan, Intelligent fault diagnosis in power systems: A comparative analysis of machine learning-based algorithms, Expert Syst. Appl. 265 (2025) 125945.

[73] T. Anwar, C. Mu, M.Z. Yousaf, W. Khan, S. Khalid, A.O. Hourani, I. Zaitsev, Robust fault detection and classification in power transmission lines via ensemble machine learning models, Sci. Rep. 15 (1) (2025) 2549.

[74] J. Ma, F.P. Dawalibi, Analysis of grounding systems in soils with finite volumes of different resistivities, IEEE Power Eng. Rev. 22 (3) (2002) 63–64.

[75] P. Calixto, Soil resistivity measurement: Two-layer model, proposed revisions to IEEE standard 80-2000 and IEEE standard 81-1983, IEEE Power Eng. Rev. 22 (4) (2002) 66–68.

[76] U. Adriano, O. Bottauscio, M. Zucca, Boundary element approach for the analysis and design of grounding systems in presence of non-homogeneousness, IEE Proc. - Gener. Transm. Distrib. 150 (3) (2003) 360.

[77] I. Colominas, F. Navarrina, Casteleiro, A numerical formulation for grounding analysis in stratified soils, IEEE Power Eng. Rev. 22 (3) (2002) 63–63.